JGR Solid Earth

RESEARCH ARTICLE
10.1029/2024JB030022

Development of Permeability Heterogeneity During Compaction of Porous Sandstone

Nicolas Brantut[1,2] and **Patrick Baud**[3]

[1]Department of Earth Sciences, University College London, London, UK, [2]GFZ Helmholtz Centre for Geosciences, Potsdam, Germany, [3]Université de Strasbourg, CNRS UMR 7063, Institut Terre et Environnement de Strasbourg, Strasbourg, France

Key Points:

- Permeability and ultrasonic wave velocities decrease during compaction of porous sandstone
- Localized compaction is co-located with strong local reductions in permeability, by around two orders of magnitude
- The connectivity of compaction bands strongly impacts permeability reduction

Correspondence to:

N. Brantut,
nicolas.brantut@gfz-potsdam.de

Citation:

Brantut, N., & Baud, P. (2025). Development of permeability heterogeneity during compaction of porous sandstone. *Journal of Geophysical Research: Solid Earth*, *130*, e2024JB030022. https://doi.org/10.1029/2024JB030022

Received 27 JUL 2024
Accepted 21 JAN 2025

Author Contributions:

Conceptualization: Nicolas Brantut, Patrick Baud
Data curation: Nicolas Brantut, Patrick Baud
Formal analysis: Nicolas Brantut, Patrick Baud
Funding acquisition: Nicolas Brantut, Patrick Baud
Investigation: Nicolas Brantut, Patrick Baud
Methodology: Nicolas Brantut, Patrick Baud
Project administration: Nicolas Brantut, Patrick Baud
Resources: Nicolas Brantut, Patrick Baud
Software: Nicolas Brantut, Patrick Baud
Supervision: Nicolas Brantut, Patrick Baud
Validation: Nicolas Brantut, Patrick Baud
Visualization: Nicolas Brantut, Patrick Baud
Writing – original draft: Nicolas Brantut, Patrick Baud

Abstract We aimed to establish how permeability heterogeneities develop in relation to compaction deformation in sandstone. Three sandstones were tested in the compactant regime: Locharbriggs sandstone, which is initially heterogeneous with beds of lower initial permeability; a low porosity (22%) Bleurswiller sandstone, which is initially homogeneous and produces localized compaction bands; a high porosity (24%) Bleurswiller sandstone, also homogeneous but producing compaction in a more diffused pattern. We monitored acoustic emission locations and elastic wave speed variations throughout deformation. In addition, at regular stages during each test, a constant pore pressure difference was imposed at the boundaries of the samples, and steady-state flow was established. Internal pore pressure measurements at four locations allowed us to derive local permeability estimates. In all samples, progressive compaction produced overall reductions in permeability. In addition, localized compaction also produced internal reorganization of the permeability structure. Strong permeability reductions in the direction perpendicular to flow, by up to two orders of magnitude, are only observed when fully connected compaction bands grow across samples. Compaction and permeability reduction preferentially impacted the more porous and permeable regions of the samples, which lead to an overall homogenization of the transport properties of the samples during deformation. Compaction results from grain crushing, and is directly linked to progressive reductions in elastic wave speed. However, the impact of compaction on permeability depends strongly on the spatial connectivity of the compacted regions.

Plain Language Summary The ability for fluids (water, gases or hydrocarbons) to flow through rocks is determined by a quantity called "permeability." In porous rocks such as sandstones, permeability changes during deformation, due to compaction of the pore space. Here, we investigated how deformation of sandstone not only reduces permeability, but also produces strong spatial variations in permeability. We tested three different sandstones, with varying degrees of initial porosity, composition, and heterogeneity. We confirmed that compaction leads to permeability reduction, but also discovered that dramatic reductions in permeability (by a factor of 100 or more) were linked to the formation of narrow, high compacted regions (called compaction bands), which developed preferentially in the highly porous regions of the samples. Our results highlight the key role of the local geometry of the compacted regions in the change of fluid transport properties rock.

1. Introduction

The development of compaction bands (CBs) in porous rocks was studied extensively in the last decades. Discrete CBs, localized features that grow orthogonal to the major principal stress and showed purely compactant deformation, were first observed in aeolian sandstone formations in Nevada and Utah (Hill, 1989; Mollema & Antonellini, 1996). Compaction localization observed in these field studies raised the attention of various communities from structural geology, mechanics, rock mechanics, volcanology, and beyond. One of the main reasons is that, as a compactive failure mode, discrete CBs constituted an alternative to cataclastic flow and, in a way, they changed the existing paradigm on the brittle ductile transition. Indeed, until the first laboratory evidences of CBs (Baud et al., 2004), the mainstream view of the brittle ductile transition in sandstone, based on laboratory studies, was that dilatancy and failure would develop at low effective pressures and cataclastic flow would develop at higher effective pressures (Wong et al., 1997). Importantly, cataclastic flow means homogeneous compaction by extensive grain crushing (Menéndez et al., 1996) and mostly isotropy when the rock experiences significant damage (Wu et al., 2000; Zhu et al., 1997). In contrast, discrete CBs are strain localization

Writing – review & editing: Nicolas Brantut, Patrick Baud

patterns and would clearly promote some anisotropy in the rock (Baud et al., 2017; Vajdova et al., 2004). Following the first observations on Bentheim sandstone, CBs were reported in various other porous sandstones (Charalampidou et al., 2011; Fortin et al., 2005; Tembe et al., 2008) for which compaction localization was in fact found to be the dominant failure mode in the compactant regime. CBs were also observed in carbonates (Abdallah et al., 2020; Rotevatn et al., 2016; Tondi et al., 2012), volcanic rocks (Loaiza et al., 2012), as well as synthetic rocks (Carbillet et al., 2021; Rice-Birchall et al., 2022), snow (Barraclough et al., 2017) and other porous structures such as polycarbonate honeycomb (Papka & Kyriakides, 1999) or metal foams (Bastawros et al., 2000).

For sandstones, field, laboratory and numerical studies reached the same conclusion that CB development would primarily occur in relatively homogeneous rock, the key parameter being the grain size distribution (Carbillet et al., 2022; Cheung et al., 2012; Schultz et al., 2010). Using a DEM Model, Wang et al. (2008) indeed showed that the local stress perturbations in the vicinity of a crushed grain or pore collapse is such that it promotes the lateral propagation of pore collapse. In a mixture of small and large grains, the propagation of the band would not extend much because crushing would preferentially develop in the smaller grains while the larger grains remained intact, as shown for gouge material by Sammis et al. (1987). Homogeneity is therefore a central question in the occurrence of compaction localization, not only because it controls the band nucleation, but also its further development and geometric attributes as suggested by Baud et al. (2015). This means that CBs could show different attributes both in field and in the laboratory, from very linear bands to the zigzag types of structures reported by Sternlof (2005). Indeed, Liu et al. (2015) concluded from numerical simulations that the shape of wiggly CBs is controlled by the mechanical properties of sandstone, which are determined primarily by petrophysical attributes, in particular grain sorting, porosity, and cementation. Despite some geometric differences, CBs reported in various studies showed some common attributes: they were observed to develop in rock with initial porosity larger than 20% and showed a comparable porosity reduction of about 15%. What is controlling these common attributes remains to date unclear.

Since the earlier work on CBs, one major interest to study this phenomenon was obviously its impact on fluid flow. For sandstone, contrasted results were obtained for both the permeability of CBs produced in the laboratory (Baud et al., 2012; Fortin et al., 2005; Holcomb & Olsson, 2003; Vajdova et al., 2004) or sampled in the field (Aydin & Ahmadov, 2009; Deng et al., 2015; Fossen et al., 2011; Sun et al., 2011). Taken together, these studies showed a permeability decrease due to CB formation ranging from less than a factor 4 up to a factor 4,000. For field samples, one could not totally rule out that the results were affected by post compaction banding changes such as cementation. However, for laboratory CBs, the differences were explained not so much by the nature of the band but by a simple geometric problem of connectivity of the CB and the formation (or not) of an efficient barrier for flow. Baud et al. (2012) showed the somehow ideal case of the anisotropic and homogeneous Diemelstadt sandstone where almost perfectly linear CBs developed through the whole sample diameter when the rock was deformed orthogonal to the sedimentary bedding. They found that in this case a permeability contrast of more than three orders of magnitude, which based on the observed geometry, could be indeed considered as a high end member value. Then, existing data suggest that for more complex geometries, the impact of CBs on permeability could be anything below this value. Compiling laboratory data, Baud et al. (2012) also suggested that the heterogeneity of the host rock via its influence on the band growth, had a fundamental control on permeability reduction. The limitation in the interpretation of the existing data is the fact that the effective permeability measured on the laboratory samples has obviously a complex relationship with the band geometries, for most cases outside the ideal situation seen by Baud et al. (2012). The broad objective of this study is therefore to clarify this relationship.

To tackle this issue, one needs to study the dynamics of CB growth and how it progressively impacts fluid flow. To follow the band growth, two strategies were used by previous studies: Acoustic emission location (notably in sandstone) (Fortin et al., 2005; Heap et al., 2015; Olsson & Holcomb, 2000; Townend et al., 2008) and in situ X-ray computed tomography (CT) (Chen, Roshan, et al., 2020; Meng et al., 2023). For CT imaging, because of the technical limitations of existing set-up together with the small sample sizes necessary to achieve a decent resolution, permeability measurements during in situ CT imaging remains a difficult challenge. This challenge was addressed successfully by Chen, Regenauer-Lieb, et al. (2020) who studied permeability changes during compaction localization in a very porous carbonate. However, due to the very large starting permeability of the studied rock and the somehow diffuse nature of compaction in their samples, the impact of CBs was not very spectacular and difficult to interpret. To our knowledge, AE location has not been used in conjunction with permeability measurements in sandstone. Despite having a rather crude resolution, this technique presents the

advantage to be performed on relatively large samples, in which different types of heterogeneity and stress-induced damage could be studied. Moreover, recent technical advances involving new pore pressure transducers (Brantut, 2020; Brantut & Aben, 2021) have lead to direct measurements of pore fluid pressure in different zones of centimetric samples, opening the potential to better map the impact of compaction localization on permeability. We therefore selected three sandstones known to develop CBs and containing different types of heterogeneities, such as bedding or porosity patches. Combining acoustic monitoring and multiple local permeability measurements, the first objective of this study was to follow very accurately the development of compaction localization and its progressive impact on fluid flow. Fortin et al. (2007) studied the influence of pore collapse and grain crushing on acoustic wave velocities. Their study focussed on hydrostatic compression, and they showed that the evolution of both the P-wave velocity (V_P) and of the S-wave velocity (V_S) reflected the competition between two mechanisms: grain crushing (meaning microcracking) leading to velocity decrease and compaction leading to the increase of the velocities. There are less data on the impact of shear-enhanced compaction and compaction localization on V_P and V_S. Fortin et al. (2005) measured together V_P and V_S and permeability during inelastic compaction of Bleurswiller sandstone. However, because of compaction localization clearly shown in their study, they could not go as far as providing a relationship between acoustic properties and permeability. Such relationship is fundamental in many applications where monitoring is involved, such as 4D seismics. With our new local permeability measurements and acoustic monitoring, the second objective of this study was to establish a clearer link between these properties.

2. Methods

2.1. Sample Materials

We tested three sandstones with similar initial porosity and mineralogical composition, that are all known to develop some degree of compaction localization when deformed at elevated confining pressure, but have different initial microstructures.

Locharbriggs sandstone, from Dumfries, south-west Scotland, has a porosity of around 24% (Jefferd et al., 2021). Its average mineralogical composition, obtained by fitting patterns of powder x-ray diffraction data, is 94%–95% quartz and 5%–6% feldspar. Bedding is not apparent at the sample size, and only a thin (around 1 mm) darker layer is visible in the lower-half of the sample we used.

Bleurville (a town also named Bleurswiller in the local alsacian dialect) sandstone, a feldspar-rich rock from the Vosges area, France, was also used. Two different blocks, quarried in the same general area but at slightly different locations, were used. One sample was cored from a block that is the same as the one called "Bleurswiller2" by Baud et al. (2015), also used by Heap et al. (2015), and has a porosity of around 24%. Heap et al. (2015) reported its composition as 66% quartz, 28% K-feldspar, 4% clays, and 2% mica. It has no visible bedding, but is known to contain millimetric lenses with locally larger porosity (e.g., Baud et al., 2015). Another sample was obtained in another block previously used by Brantut (2018) and Jefferd et al. (2021), which was simply referred to as "Bleurville sandstone" but will be called here "Bleurswiller3" to avoid further confusion. The mineralogical composition of Bleurswiller3, obtained from powder x-ray diffraction data, is of around 81 ± 2% quartz, 12% feldspar and 7 ± 2% mica. It appears to be more visibly homogeneous than Bleurswiller2, and has an initial porosity of around 22%–23%. Samples of 40 mm in diameter and 100 mm in length were cored perpendicular to bedding, and end faces were ground to ensure parallelism. The samples were kept dry at 60°C in an oven prior to experiments.

2.2. X-Ray Computed Tomography

The initial structure of each sandstone type was determined using X-ray computed tomography (CT). For each sandstone, we cored an additional sample in the same block, in the same orientation, and in the immediate vicinity (a few cm apart) of the sample that was used in the triaxial deformation experiment. X-ray CT imaging on these additional samples was performed at the High-Resolution CT Facility at the University of Texas at Austin, following a procedure detailed by Louis et al. (2009). The voxel size was 20.7 × 20.7 × 20.7 μm^3. The reconstructed images are formed from 4,836 horizontal slices, each of which is made of 2007 × 4847 voxels. From the image data, we computed average density profiles using the technique of Louis et al. (2009). The method consists of calibrating voxel gray levels using selected volumes containing materials with three known densities: (a) pure quartz, (b) open void, and (c) the total average density of the entire rock.

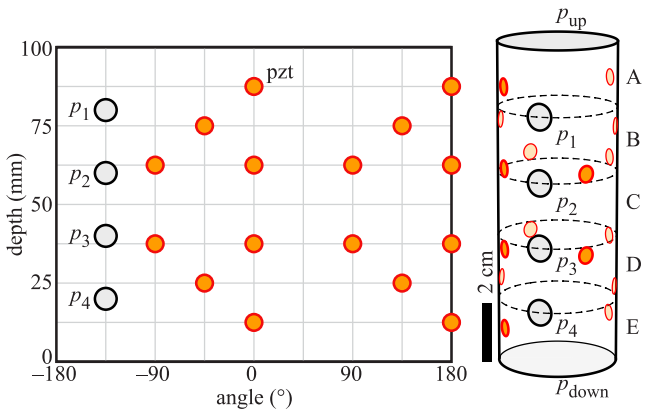

Figure 1. Schematic of sensor positioning around the sample surface, showing the 16 piezoelectric transducers (orange) and four pore pressure sensors (gray). The position of the pore pressure transducers defines five layers, denoted A–E, from the upstream end to the downstream end of the sample.

2.3. Instrumentation

Each sample was jacketed in a perforated 3 mm thick nitrile sleeve. The sleeve was equipped with a set of 16 aluminum inserts mounted with piezoelectric ceramic rods polarized perpendicular to the sample surface (Figure 1). In addition, four miniature pore pressure transducers (Brantut, 2020; Brantut & Aben, 2021) were positioned at regular vertical positions along the sample, subdividing the sample into five regions (Figure 1).

The 16 piezoelectric transducers were connected to 40 dB, band-pass pre-amplifiers (100 kHz–1 MHz). The amplified signals were connected to a logic unit that triggered waveform recording if a threshold of 150 mV was overcome on more than two channels within a time window of 10 μs. Waveforms of 4,096 samples from all 16 channels were recorded at 50 MHz sampling rate. Due to the low throughput of the digital oscilloscopes, a maximum of five events per second could be recorded, missing potential other events.

In addition to the passive recording of acoustic emission events, we also conducted regular active ultrasonic wave velocity surveys at regular time intervals throughout the experiments. During a survey, each sensor was sent a 250 V, 1 MHz impulse to generate an ultrasonic source, and the resulting waveforms were stacked and recorded at 50 MHz on the remaining 15 sensors.

2.4. Deformation Tests

Deformation tests were conducted in the Triaxial Rock Physics Ensemble installed at University College London (Eccles et al., 2005). Confining pressure was applied by pressurizing silicone oil with an electric pump and was maintained at any set point within ±0.4 MPa. Pore fluid pressure (distilled water) was imposed at either or both ends of the sample by a servo-controlled intensifier, with a precision of 0.001 MPa. Pore volume was measured by monitoring the piston displacement inside the intensifier. At constant pore pressure, fluctuations of the order of 0.01 cc were observed due to thermal effects. Axial deformation was imposed by a servo-hydraulic ram, and load was measured externally with a load cell, and corrected from piston friction. Axial shortening was also measured externally by two Linear Variable Differential Transformers, and corrected from elastic distortion of the loading column. In this paper we used the convention that the compressive stresses and compactive strains (i.e., shortening) are considered to be positive. All the mechanical data were recorded at 1 Hz.

The jacketed samples were placed between stainless steel pore pressure distribution plates, and then between steel end-caps inside the pressure vessel. After the vessel was closed, confining pressure was raised to 10 MPa and let to equilibrate for around 1 hr. The sample was saturated by setting an upstream fluid pressure to $p_{up} = 1$ MPa while the downstream end of the sample was vented to the atmosphere. After around 100 cc of water was flushed through the pore pressure system and sample, the downstream end of the sample was connected to the intensifier and a uniform pore pressure of 0.5 MPa was imposed. The confining pressure was raised in steps up to 80 MPa. Deformation tests were conducted at a nominal axial strain rate of 10^{-5} s^{-1}. Permeability measurements were conducted at each confining pressure step prior to deformation, and at regular strain intervals during deformation. The procedure consisted of (a) stopping axial deformation if needed, (b) venting the downstream end of the sample to the atmosphere while maintaining a constant pore pressure at the upstream end, (c) repeating the operation with flow in the reverse direction, and (d) reconnecting both ends to the intensifier to reequilibrate to a homogeneous pore pressure within the sample. During each flow-through step, we waited until a constant flow rate and constant internal fluid pressures were achieved before reversing the flow direction. Direct application of Darcy's law was used to compute the average sample permeability, as well as the average permeability within each of the five subregions delimited by the locations of the pore pressure sensors.

2.5. Data Processing

Waveform data from ultrasonic surveys were processed to obtain relative variations in P-wave velocities during deformation. One "master" survey (containing data from all 16 sources) was chosen, and first arrivals were picked manually to obtain a set of absolute V_P between each transducer pair (assuming straight ray paths). The accuracy

in V_P was of the order of 200 m/s (around 5%). Then, we tracked the change in arrival times between each trace of subsequent surveys using cross-correlation of resampled waveforms in time windows centered around the first arrival, which leads to a precision of the order of 0.1%. The waveforms recorded by the trigger system were processed to obtain acoustic emission (AE) event locations. First arrivals were automatically picked using a method based on the Akaike Information Criterion Sleeman and van Eck (1999), and manually corrected when necessary. We used the P-wave velocities measured during ultrasonic surveys to build a time-dependent homogenized, anisotropic (elliptical) velocity model, and located each AE event using a collapsing grid-search method with least-absolute value criterion. The AE location accuracy was difficult to assess due to the nonlinearity of the forward problem and the approximate nature of the velocity model. By trial-and-error, moving manual first arrival picks within a reasonable visual range (typically within a 1 μs time window), we find variations in event locations of the order of ±2 mm.

The pore pressure transducers were calibrated using a linear regression of the voltage measured at different confining and pore pressures, during stages where pore pressure was uniform within the sample (Brantut & Aben, 2021). This absolute calibration was accurate to within 0.1 MPa. For the computation of local permeability during each flow-through stage, we corrected the pore pressure records for any potential offsets, using the imposed intensifier pressure as reference for the homogeneous internal pore pressure prior to flow.

To compute the local permeability in each layer, we assumed one dimensional steady flow along the vertical axis, and used the local pore pressure gradients in a direct application of Darcy's law:

$$k_i = \frac{q\eta}{A}\frac{\Delta p_i}{L_i}, \tag{1}$$

where k_i is the permeability in layer i, q is the measured flow rate across the sample, A is the sample cross-sectional area, η is the viscosity of water, Δp_i is the pore pressure difference across the layer, and L_i is the layer thickness. In principle, with one side vented to atmospheric pressure, the pore pressure profile $p(z)$ during steady flow in one direction should be equal to $P_{up} - p(z)$ during flow in the reverse direction, where P_{up} is the upstream pore pressure. In addition, flow rates should be equal in magnitude. Thus, in an ideal scenario we could average the flow rate and pore pressure profiles to improve our permeability estimates. In practice, we found that the determination of local permeability (using Equation 1) was not always possible due to measurement errors that lead to unphysical negative pore pressure gradients; this was especially the case in strongly heterogeneous samples, where pore pressure differences across layers could be of the order of 0.01 MPa. Thus, the local permeabilities reported here were not obtained by averaging pore pressure profiles, but rather using only the data set (forward or reverse flow) that lead to the most reliable permeability estimates. Even with this data selection procedure, the permeability in the central layer of the Locharbriggs sample could not reliably be computed, since the pore pressure gradient was too small to be measurable. The assumption of one-dimensional flow along the sample axis becomes invalid if horizontal heterogeneities appear, as in the case of inhomogeneous compaction. In this case, our measurement method produces estimates of the effective permeability within any given layer, that is, the average permeability that would produce the observed pressure gradient along the vertical axis.

2.6. Microstructural Analysis

After deformation, the samples we impregnated with epoxy, cut longitudinally and polished with SiC down to #3000 grit and then with a diamond suspension down to 1 μm. The polished sections were then carbon coated and observed with a Scanning Electron Microscope (JEOL JSM 6480) in backscattered electron mode with an accelerating voltage of 15 kV.

3. Results

3.1. Locharbriggs Sandstone

Figure 2a presents a CT image of an intact sample of Locharbriggs sandstone. The density profile obtained from gray level calibration (Figure 2b) reflects the presence of denser bands in various areas of the sample. In particular, in the lower half of the sample, the thin dark layer that was visible with the naked eye appears much denser than average. In areas without bands (e.g., Figure 2c), the average density corresponds to an estimated porosity of 28% (using the solid density of the average mineralogical composition of the rock). In the high density

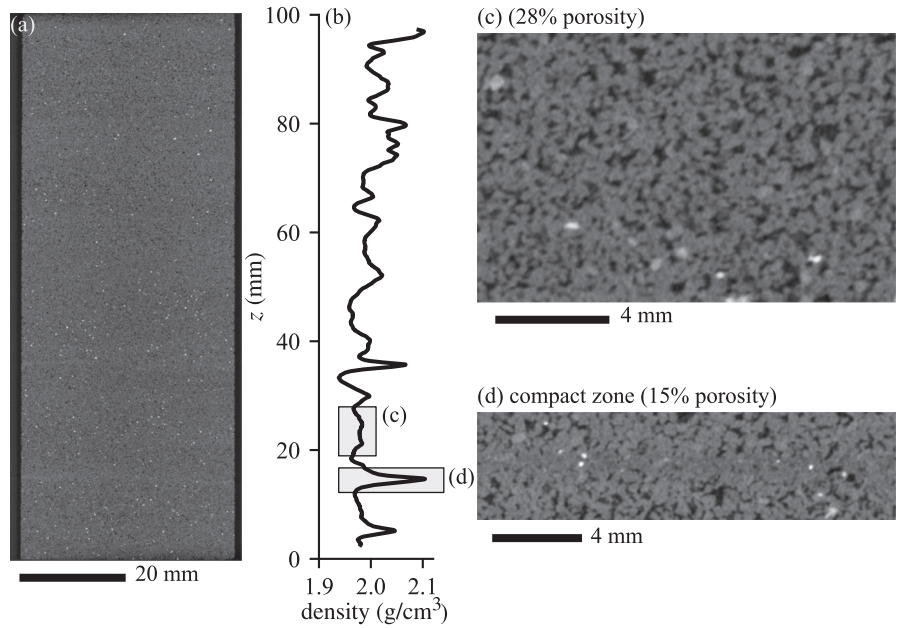

Figure 2. X-ray CT image and density profile in intact Locharbriggs sandstone. (a) Vertical cross section of the full sample. (b) Density profile obtained from gray level calibration (see Section 2). (c) High porosity region without noticeable bedding heterogeneity. (d) Low porosity region containing a thin compact bed.

band, the porosity is more difficult to infer because of the visible compositional difference. Selecting several small band segments such as the ones presented in Figure 2d, we inferred a porosity of 15% for these denser parts of the sample.

The initial horizontal P wave velocity of Locharbriggs sandstone ranges from 3.4 to 3.7 km/s at 10 MPa effective confining pressure, and increases up to 3.8–4.1 km/s at 100 MPa (Figure 3a). The initial heterogeneity is not strong, will all measurements remaining within the error range of the measurement technique. By contrast, the average permeability of Locharbriggs sandstone is mostly independent of confining pressure (Figure 4a). The local permeability estimated using Equation 1 at the highest tested confining pressure is strongly heterogeneous: the pore pressure profile during flow indicates that permeability is of the order of 10^{-14} m^2 in the upper layers (above a depth of 20 mm) of the sample (Figure 4b). By contrast, the permeability of the lowermost region is of the order of 10^{-16} m^2. Thus, it is the permeability of that layer that controls the average across the sample. This low permeability region contains the thin layer with a porosity of 15% identified in the CT scan: this thin layer is thus likely to be a substantial barrier to fluid flow.

The sample of Locharbriggs sandstone was deformed at $P_c = 102$ MPa and a homogeneous pore pressure of $P_f = 1$ to 5 MPa. Under those conditions, the behavior was macroscopically ductile (Figure 5a). The differential stress initially increased linearly with increasing axial strain, and at around 1.3% strain it reached a constant plateau of around 145 MPa. The sample yielded in compaction, and porosity decreased steadily with increasing strain, by around 2% at 3% strain. At large strain, the rate of porosity change approaches the rate of sample shortening, indicating limited radial strain.

The average permeability across the sample remained stable up to axial strains of around 1.2% (Figure 6a), and then experienced a decrease by around one order of magnitude from 10^{-15} m^2 down to around 10^{-16} m^2 as axial deformation reached 2%. Beyond that point, the average permeability remained stable. The decrease in average permeability between 1% and 2% strain is the result of strongly heterogeneous local permeability variations. In layer A, permeability decreases smoothly by a factor of 2 to 3. In layer E, the decrease is of the order of a factor 10. By contrast, the permeability in layer D decreases by almost two orders of magnitude, starting at around 10^{-14} m^2 and dropping to just above 10^{-16} m^2 at 2% strain. Since the permeability in layer E is much smaller than in any other layers, the average permeability mostly follows the one in that layer. Past 2% strain, permeability in all layers stabilizes. All P wave velocities measured along horizontal paths (perpendicular to the compression axis)

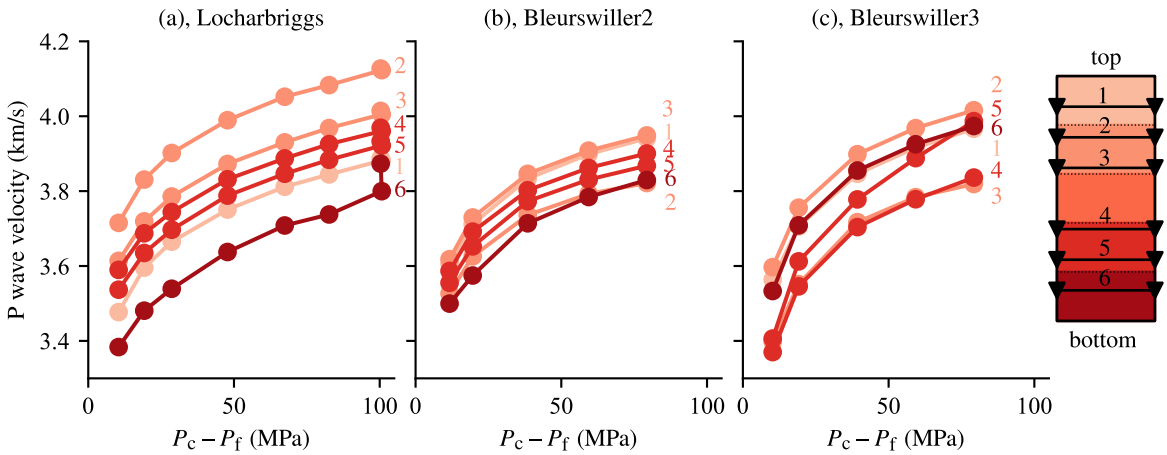

Figure 3. Evolution of horizontal P wave velocities of intact Locharbriggs (a), Bleurswiller2 (b) and Bleurswiller3 (c) sandstone as functions of effective confining pressure. Each curve is labeled with a path number and color corresponding to different positions along the sample axis. The absolute error of each wave velocity measurement is of the order of 0.2 m/s, mostly due to the manual picking procedure of the reference waveforms (See text for details).

decreased throughout deformation (Figure 6a). The decrease is initially homogeneous and modest, with a drop of around 2% at 1.2% axial strain. Beyond that point, the decrease becomes heterogeneous. In layers A and B (paths 1, 2, and 3), P wave velocities decrease at a constant rate by a further 1%–2% at 3% strain. Along path 6 (layer E), P wave velocity decreases abruptly by about 1% at 1.6% strain, and then decreases steadily by a further 3% over the next 2% strain. The P wave velocity in the upper part of layer D (path 4) also decreases abruptly at 1.6% strain, and keeps decreasing severely with increasing strain, reaching −15% at the end of the test. Along path 5 (lower part of layer D), the decrease accelerates progressively 1.6% strain, and reaches a substantial 12% at the end of the test.

AE locations show strongly localized patterns (Figure 7). Up to around 1% strain, AE events were mostly concentrated near the top and bottom ends of the sample. Between 1% and 1.5% strain, AE activity persisted at both ends of the sample, slightly propagating away from the boundaries into layers A and E. In addition, we observed a clear concentration of AE events along a planar, horizontal feature located near the top of layer D. This structure did not span the entire width of the sample (see N-S section). In the same strain interval, we also observed a smaller AE cloud with limited horizontal extent at the boundary between layers C and D. With increasing deformation, between 1.5% and 2% axial strain, we observed a sharp concentration of AE events in layer D and the lowermost part of layer C, organized into four horizontal structures. The structure initiated in the previous strain interval extended completely across the sample width, and some of the other distinguishable structures also appeared to be through-going. Another narrow horizontal AE cloud appeared in the following strain interval (2%–2.5%), but was not completely through-going (this is visible in the N-S section). Some minor AE activity persisted in previously active regions. Between 2.5% and 3% strain, AE activity was localized in a small horizontal patch in the lower part of layer A, as well as in a more diffuse region at the bottom of layer D. Beyond 3% strain, AE activity remained very limited. The regions of localized AE activity coincide with areas where the wave speed decreased most. This is especially visible in the evolution of $\Delta V_p/V_p$ along path 4 (layer D, Figure 6a), which decreased sharply between 1.5% and 2% strain, while most AE activity was focused in the same region. This is also the same region that experienced the largest drop in permeability, in the same strain interval. In general however, the relationship between AE activity and the measured permeability drop within a given layer depends strongly on the lateral extent of the AE cloud: when the AE cloud did not span the entire width of the sample, no significant permeability change could be observed.

3.2. Bleurswiller (2)

Bleurswiller2 appears homogeneous at the sample scale (Figure 8), without clear layering in terms of porosity. However, there are local regions of a few mm in size that have locally large porosity contrasts (up to 5%) with the bulk. These porosity patches have been previously reported in this rock type by Fortin et al. (2006) and Baud et al. (2015).

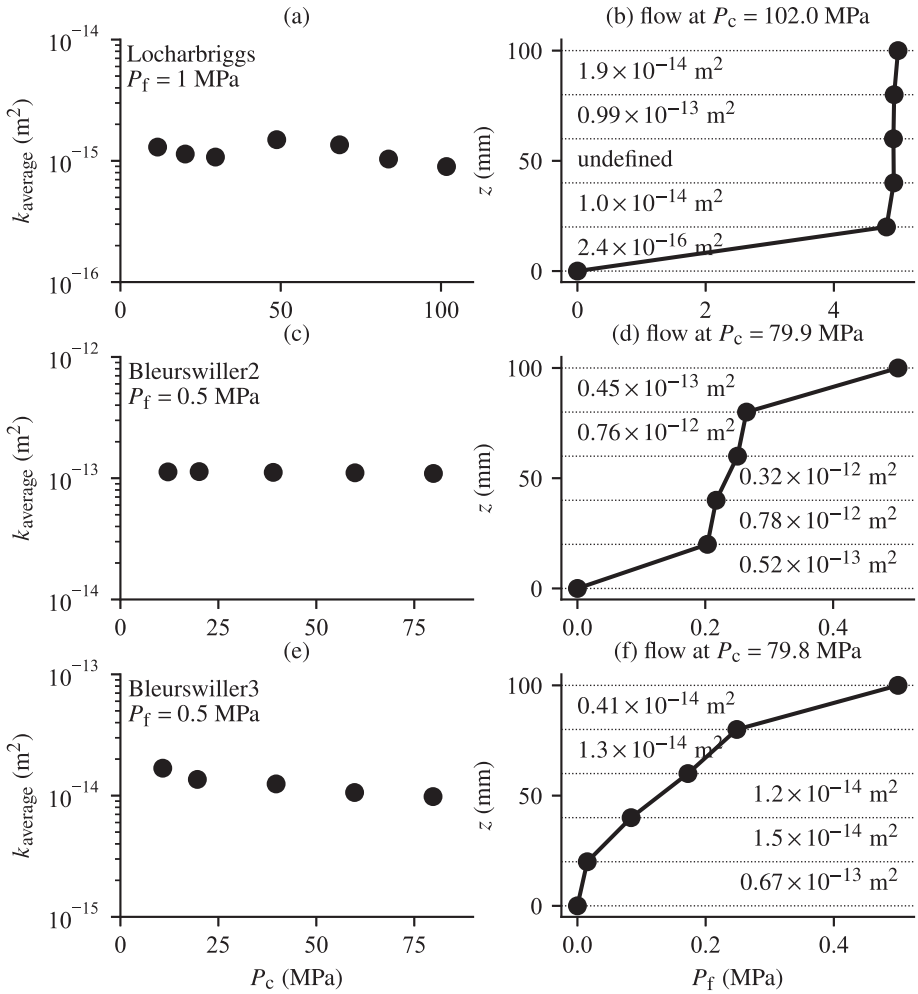

Figure 4. Permeability evolution and structure of intact (a, b) Locharbriggs, (c, d) Bleurswiller2 and (e, f) Bleurswiller3 sandstone. (a, c, e) Average sample permeability with increasing confining pressure, and (b, d, f) vertical pore pressure profile during steady flow at the highest confining pressure, using a constant upstream pore pressure (5 MPa for Locharbriggs sandstone, and 0.5 for Bleurswiller2 and 3 sandstones) and a vented downstream. In Locharbriggs, sandstone, the pore pressure gradient across layer C was so small that measurement errors lead to a unphysical negative permeability values; local permeability was thus not accessible.

The horizontal P wave velocity of intact Bleurswiller2 sandstone is uniform across the sample, with an average of 3.57 km/s at 10 MPa effective confining pressure and an increase up to 3.88 km/s at 80 MPa (Figure 3b). The average permeability of Bleurswiller2 sandstone is around 10^{-13} m^2, and is independent of confining pressure (Figure 4c). The pore pressure profile indicates a heterogeneous permeability structure, with top and bottom layers having a low permeability of around 0.5×10^{-13} m^2, and the central part of the sample being around 10 times more permeable (Figure 4d). The sample of Bleurswiller2 sandstone was deformed at $P_c = 80$ MPa and $P_f = 0.5$ MPa. The mechanical behavior was typical of the ductile regime, with a differential stress plateau at around 110 MPa together with steady compaction at strain >1% (Figure 5c). During the stress plateau, the axial strain was almost equal to the compactant change in porosity, indicating nearly uniaxial strain state.

The average permeability was initially stable during the elastic loading stage, up until around 1% strain, beyond which it gradually decreased with ongoing strain (Figure 6b). The largest permeability decrease was observed in layers B and D, dropping by around two orders of magnitude in the interval from 1% to 2.5% strain. In the top and bottom layers (A and D), permeability decreased gradually by only about a factor 2 over the entire experiment. In the centermost part of the sample (layer C), permeability also decreased slightly by around a factor 2 from 2% to 2.5% strain, and decreased further between 3% and 3.5% strain. The most striking result observed in this sample is

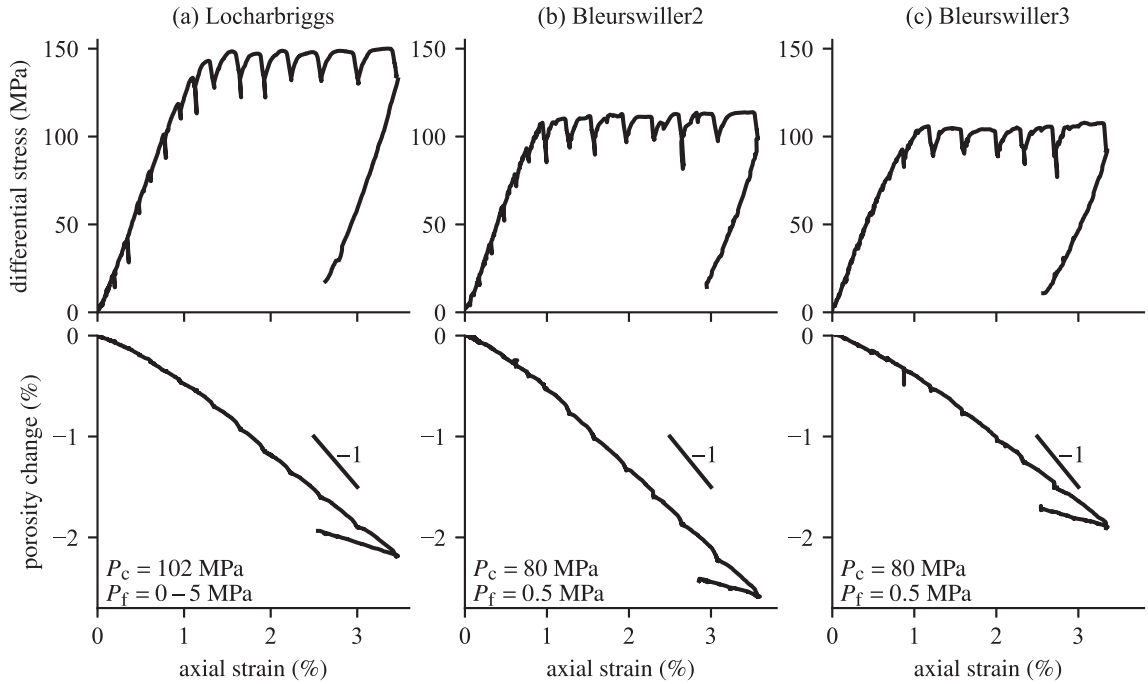

Figure 5. Mechanical behavior of the three tested sandstones: stress-strain and porosity change in (a) Locharbriggs sandstone deformed at P_c = 102 MPa and P_f from 1 to 5 MPa, (b) Bleurswiller2 sandstone deformed at P_c = 80 MPa and P_f = 0.5 MPa, and (c) Bleurswiller3 sandstone deformed at P_c = 80 MPa and P_f = 0.5 MPa. The regular differential stress drops correspond to stress relaxation during intervals when deformation was stopped (axial piston locked) and permeability was measured.

that the permeability in layers B and D was initially one order of magnitude larger than that in A and E, but after 3% strain the reverse was observed.

A decrease in horizontal P wave velocity was observed along all paths (Figure 6b). The decrease was initially homogeneous in all layers up until around 1% strain. Beyond that point, the velocity dropped sharply along path 2 (uppermost region in layer B). Similarly, at 1.5% strain, a sharp drop was observed along path 5 (layer D). At strains>2%, the rate of velocity decrease stabilizes along all paths. The velocity variations were strongly localized, with neighboring paths that had markedly different evolutions. For instance, while a drop of about 9% is recorded along paths 2 between 1% and 2% strain, the velocity along path 3 (only 12.5 mm above path 2) decreased only by about 2% in the same strain interval. The regions that experienced the strongest decrease in wave velocity were the same as those that experienced the strongest decrease in permeability (layers B and D).

The AE locations show a concentration of AE activity in two separate regions that correspond to layers B and D (Figure 9). The AE activity within layer B initiated between 0.5% and 1% strain, and occurred as two sub-horizontal clusters than grew into a layer-wide horizontal region going through the entire sample diameter during the 1%–1.5% strain interval. In layer D, the AE activity proceeded in a similar fashion, with an initiation of two sub-horizontal clusters between 1% and 1.5% strain, and an extension of these clusters throughout the layer in the subsequent strain interval. Beyond 2% strain, AE activity continued at a lower overall rate, with AE events dominantly localized at the border of the regions that contained the initial clusters: the AE locations extend gradually into previously inactive regions.

Overall, in the Bleurswiller (2) sample, permeability and wave velocity dropped jointly in the regions where most of the AE activity was concentrated.

3.3. Bleurswiller (3)

The structure of the undeformed sample of Bleurswiller3 sandstone, shown in Figure 10a, is marked by a large area (bottom 3/4 of the sample) of homogeneous material, with an average porosity of 22% (Figure 10d). By contrast, the upper part of the sample (about a quarter) is clearly denser (Figure 10b) and includes a larger proportion of denser minerals. Within this region, we observed the presence of subhorizontal layers of less porous

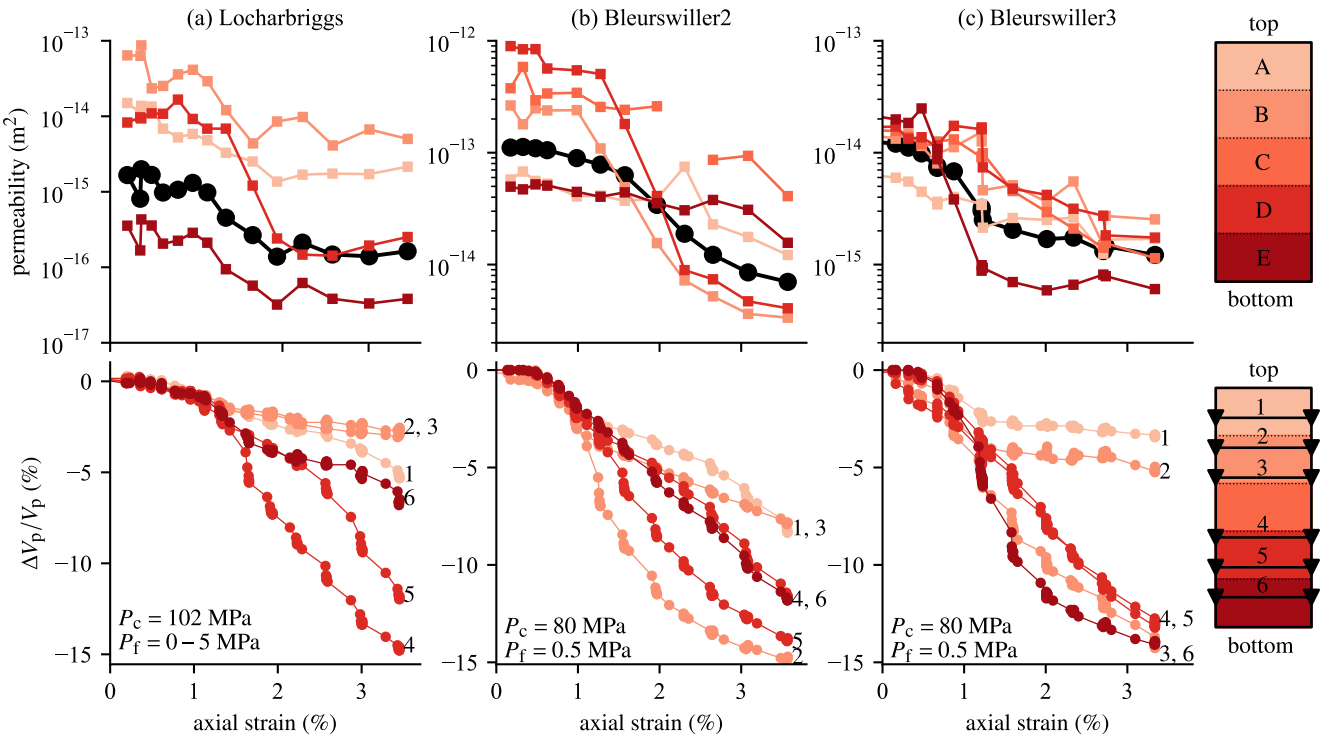

Figure 6. Evolution of permeability and horizontal wave velocities during deformation. (a) Locharbriggs sandstone, (b) Bleurswiller2 sandstone, (c) Bleurswiller3 sandstone. The black curves show the average permeability across the entire sample. All curves are color-coded to match each layer from A (light red) to E (dark red). P wave velocities along horizontal paths are numbered from 1 (top) to 6 (bottom). In Bleurswiller2 sandstone, the permeability at 2.3% in layer C could not be computed because the pore pressure measurements indicated an unphysical, negative pressure gradient in that interval. This error is also likely impacting the permeability inferred in other layers at that strain, with an unexpected increase in layer A. In all rocks, the initial permeability (at zero strain) reported in each plot might differ slightly from that reported in Figure 4 because the measurements were conducted approximately 1 day apart, during which some time-dependent compaction may have occurred.

beds, lined with denser minerals (most likely oxides) (Figure 10c). The mineralogical composition of the denser parts is clearly different from that of the bulk rock, so that we excluded the denser grains (white grains in Figure 10c), and then used the mineralogical composition of the bulk solid in order to infer the porosity from density data. The resulting average porosity of the denser region was of around 16%. The initial horizontal P wave velocity of Bleurswiller3 sandstone is very similar to that of Bleurswiller2 sandstone, with a low degree of heterogeneity across the sample (variations well within the measurement error), and an average of 3.63 km/s at 10 MPa effective confining pressure and an increase up to 3.96 km/s at 80 MPa (Figure 3c). The average permeability of Bleurswiller3 sandstone is around 10^{-14} m^2, and decreased mildly (by a factor of 2) with increasing confining pressure (Figure 4e). During steady flow, the pore pressure profile shows a strong heterogeneity in permeability (Figure 4e), with the uppermost layer being around one order of magnitude less permeable than the lowermost layer.

The mechanical behavior was very similar to that of Bleurswiller2 deformed in the same conditions, with a stress plateau at around 105 MPa. Compaction was also observed throughout deformation, but was quantitatively smaller than in Bleurswiller2. A substantial fraction of the imposed axial strain was not accommodated by a porosity decrease, which implies a departure from purely uniaxial strain geometry.

The permeability change is very limited during deformation up to an axial strain of 0.8%, with a slight decrease recorded in layer A and E (Figure 6c). Between 0.8% and 1.2% strain, a strong decrease in permeability, by around one order of magnitude, was recorded in layer E. The permeability remained stable in the other layers. At 1.2% strain, we conducted two permeability measurements: one immediately following the arrest of the piston, and one after around 1 hr of relaxation. An axial strain of 0.02% was accumulated during that 1 hr interval. The permeability in layers A, B, and D was substantially lower in the second measurement, which indicates that the small strain developed during stress relaxation was associated to significant microstructural changes that impacted fluid flow. With further strain, we observed a stabilization of the permeability in layer A, B, and E, while

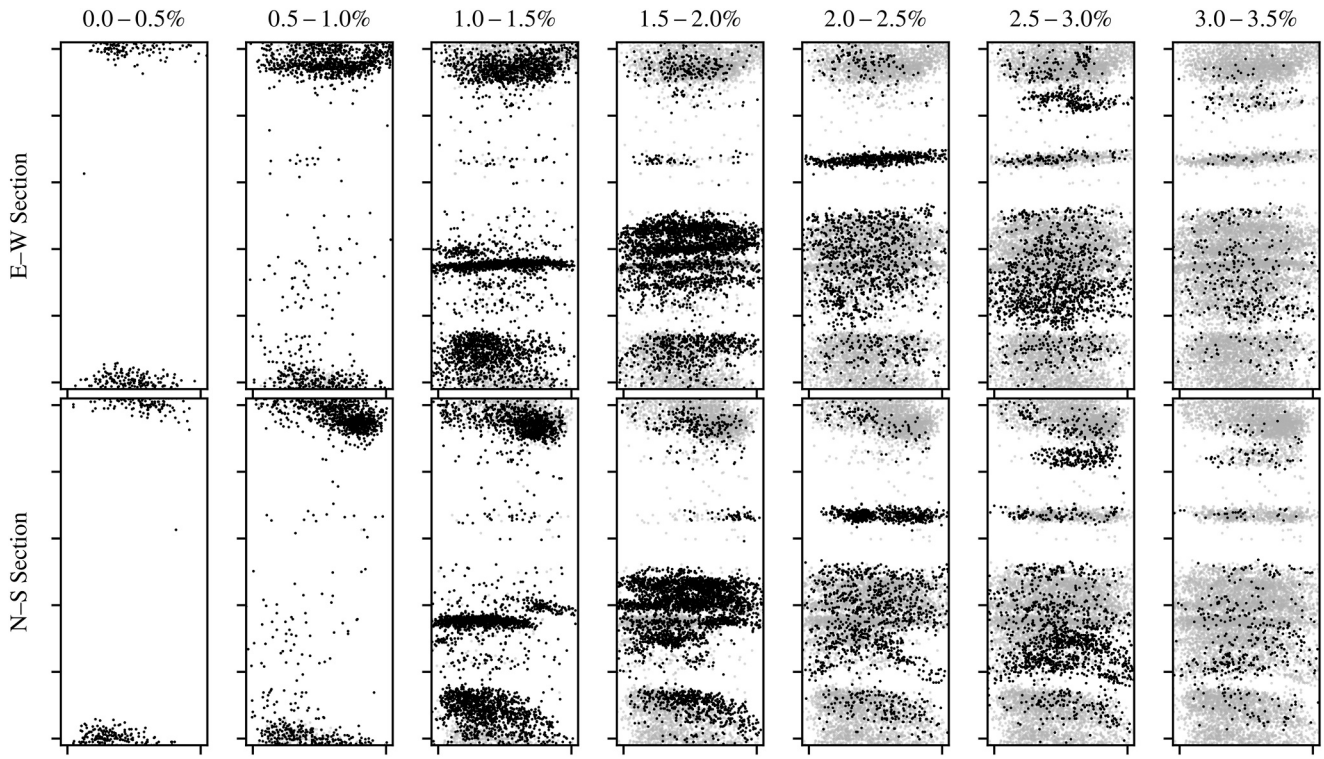

Figure 7. Acoustic emission locations during deformation of Locharbriggs sandstone. For each strain interval, black markers show locations of events that occurred during the interval, and gray markers show locations of events that occurred during all previous intervals.

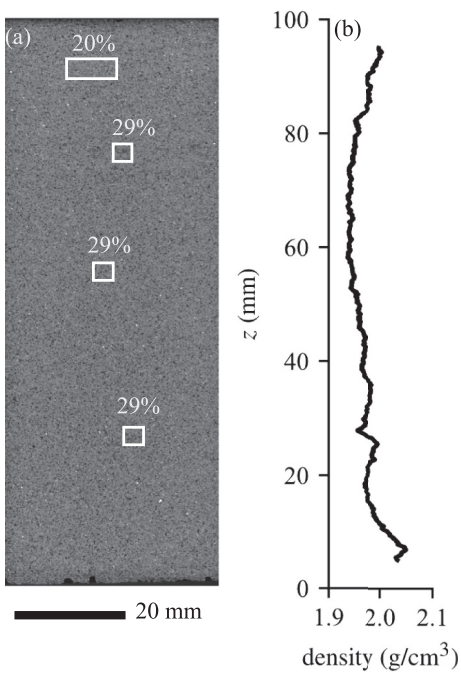

Figure 8. X-ray CT image (a) and estimated density profile (b) of Bleurswiller2 sandstone. Patches with large porosity contrasts are highlighted in white rectangles in (a).

layers C and D became progressively less permeable. After 3.3% strain, the average permeability was around 10^{-15} m^2, that is, approximately one order of magnitude smaller than in the intact rock. The lowermost layer (E) was the least permeable (around 6×10^{-16} m^2, dropped from 2×10^{-14} m^2), whereas layer B, which was initially the least permeable (6×10^{-15} m^2), had retained the largest permeability value (2×10^{-15} m^2). Thus, similarly to the case of Bleurswiller2, the initially most permeable layers were those most impacted by deformation. The horizontal P wave velocities decreased by 2%–4% at axial strains up to 1%. Beyond that point, a sharp decrease was observed along paths 3 and 6, that is, in the lower part of layer B and in layer E, with drops of 8% and 10% at 1.5% strain, respectively. Wave velocities along those paths decreased at a lower rate with ongoing strain, reaching −14% at 3.3% strain. By contrast, along paths 4 and 5 (in layer D), the velocity decreased steadily throughout deformation, with a recorded drop of 13% at the end of the test. In layers 1 and 2 (layer A and upper part of layer B), the velocity barely changed with increasing deformation beyond 1% axial strain.

Very little AE activity was recorded at strains up to 1% (Figure 11), with only few distributed events throughout the sample volume. Between 1% and 1.5% strain, AE events were detected in three main regions. One cluster of events occurred in layer E, relatively diffused throughout this layer. Another cluster was detected in the upper part of layer D, with a slight concentration of events along a horizontal region. Another group of events was detected at the interface between layers B and C and within layer C itself, with also a concentration of events along a horizontal structure. By contrast with the AE locations reported for Locharbriggs and

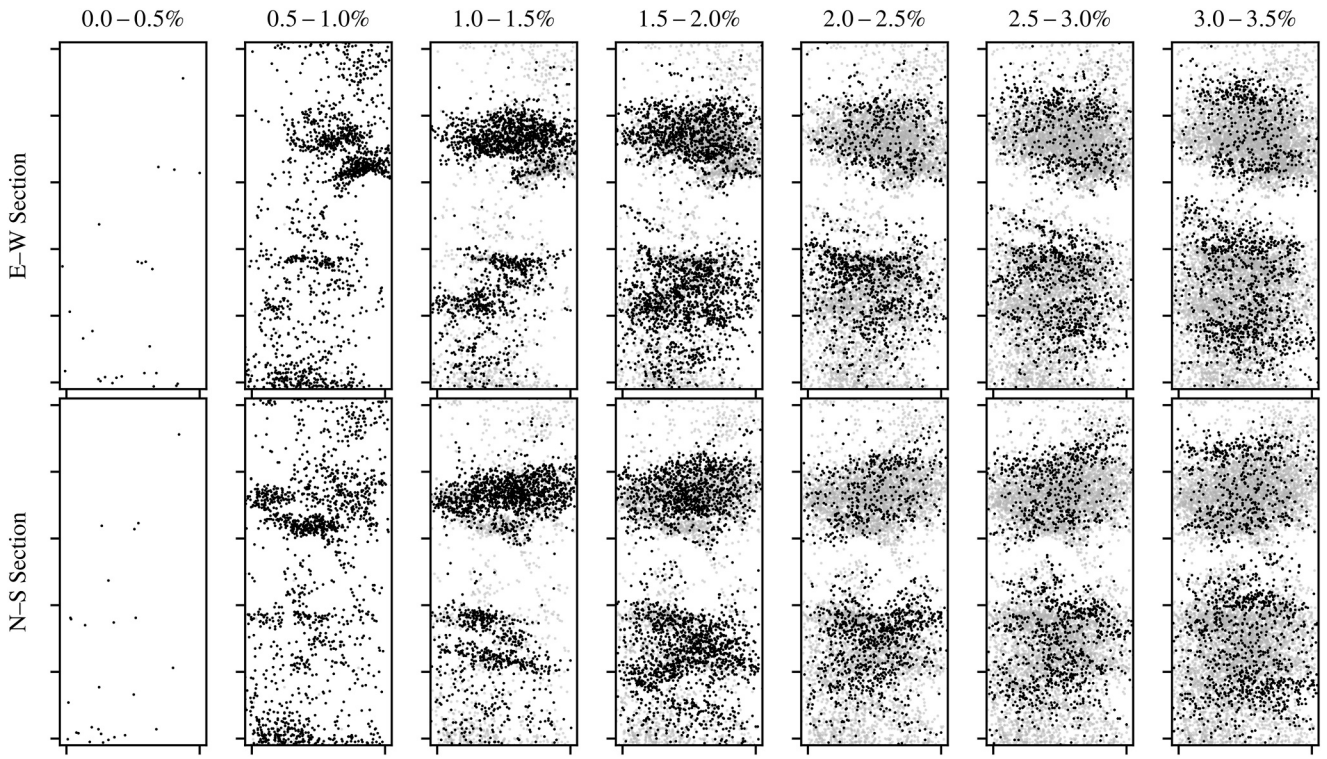

Figure 9. Acoustic emission locations during deformation of Bleurswiller2 sandstone. For each strain interval, black markers show locations of events that occurred during the interval, and gray markers show locations of events that occurred during all previous intervals.

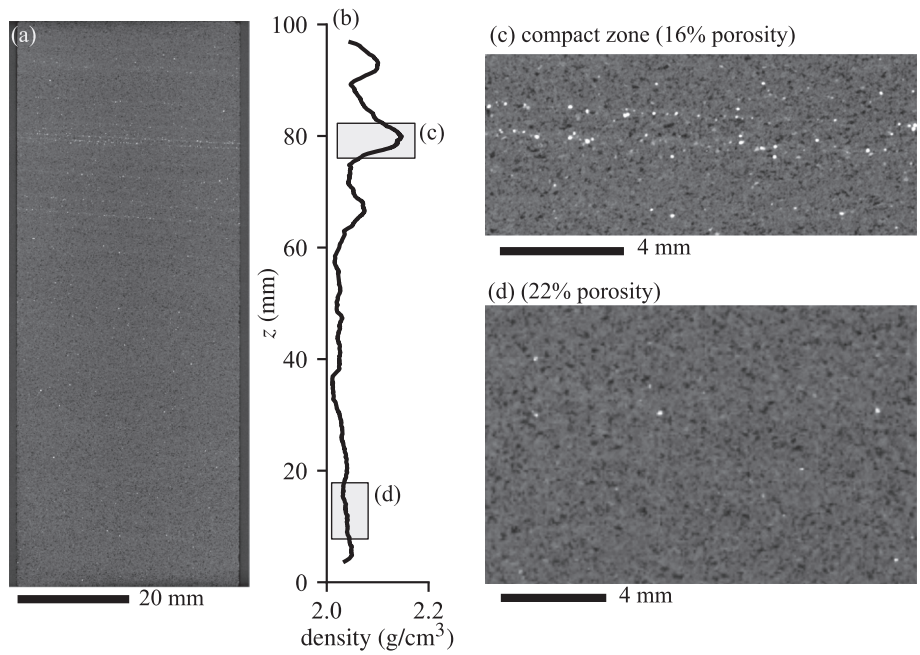

Figure 10. X-ray CT image and density profile in intact Bleurswiller3 sandstone. (a) Vertical cross section of the full sample. (b) Density profile obtained from gray level calibration (see Section 2). (c) Low porosity region with bedding heterogeneity. (d) High porosity homogeneous region.

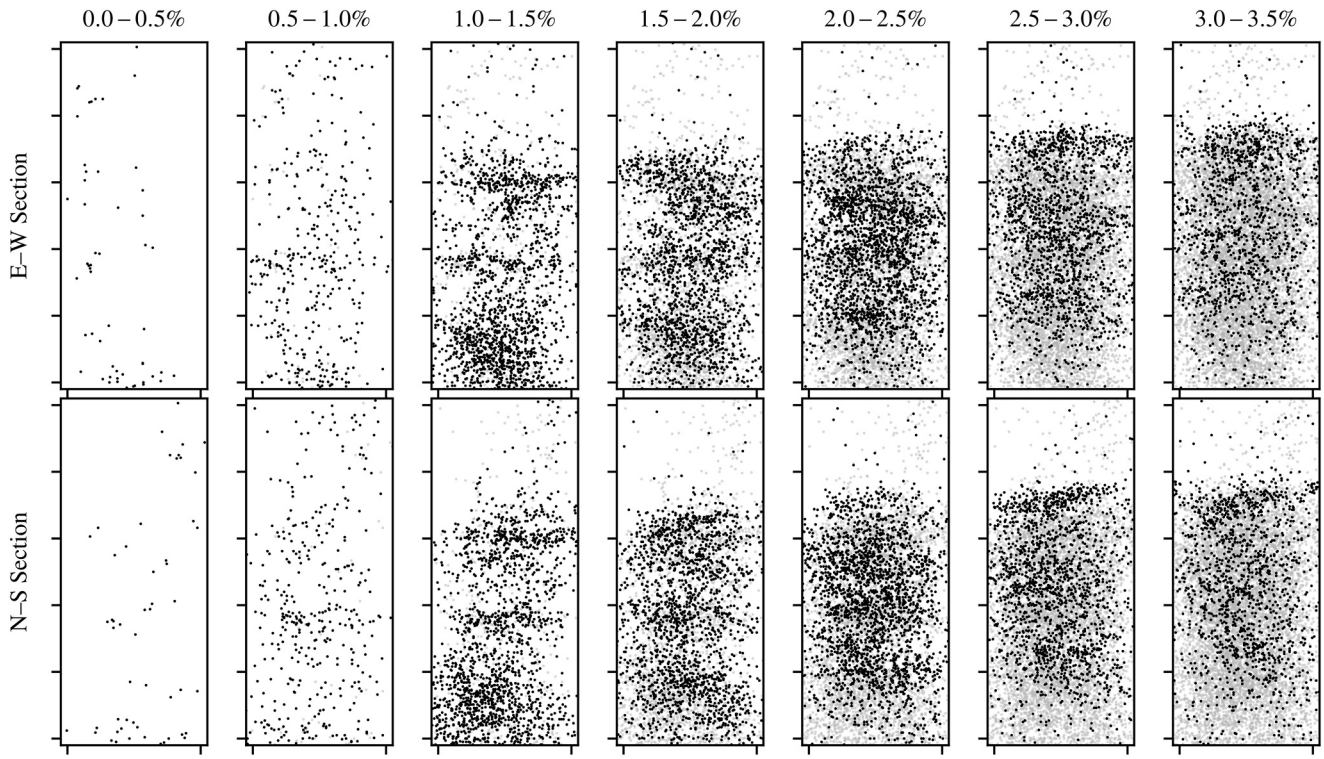

Figure 11. Acoustic emission locations during deformation of Bleurswiller3 sandstone. For each strain interval, black markers show locations of events that occurred during the interval, and gray markers show locations of events that occurred during all previous intervals.

Bleurswiller2 sandstones, AE events in Bleurswiller3 do not delineate as clearly any horizontal structures. This could be due in part to poorer accuracy in AE locations; refining the images of Figure 11 using stricter rejection criteria in terms of location errors (i.e., excluding poorly located events) does not change the more diffuse nature of the AE clusters seen in the 1%–1.5% strain interval. With increasing strain, the AE activity continued in the same regions, expanding into previously inactive parts, but without a clear concentration of events along horizontal bands. Between 2.5% and 3% strain, a new AE cluster appeared along a sub-horizontal, slanted, south-dipping region within layer B, while AE activity almost stopped in layer E. Throughout the test, no substantial activity was recorded in layer A. In Bleurswiller3, similarly to Bleurswiller2 and Locharbriggs sandstone, we observed a high degree of consistency between the different physical measurements: permeability decreased most in layers where AE activity was concentrated and in which horizontal P wave velocity decreased most.

4. Deformed Microstructures

As anticipated from AE locations and local permeability and wave speed measurements, the deformed Locharbriggs sandstone shows a strong microstructural heterogeneity, with regions left practically undeformed (Figure 12a). Discrete compaction bands can be observed (Figure 12b): these are subhorizontal, anastomosing layers of two to three grains in width (a few 100 μm) where the grains a systematically crushed to various degrees (Figure 12b). We see axial splitting of large grains, Hertzian cracks at grain contacts, and a filling of the existing porosity with fine, angular particles. A substantial region of the sample exhibits widespread grain crushing, and individual bands cannot be clearly distinguished (Figure 12c). In the lowermost region of the sample, which hosts the dark, low porosity layer detected in the CT scans and is associated with low permeability, we clearly observe a single low porosity layer made of interpenetrating grains and fine-grained oxides (Figure 12d). This layer appears weakly impacted by deformation, and only a few axial cracks, not necessarily through-going, can be observed across it. The neighboring regions above and below are impacted by deformation just like the remainder of the sample, for example, with the presence of localized compaction bands (Figure 12d).

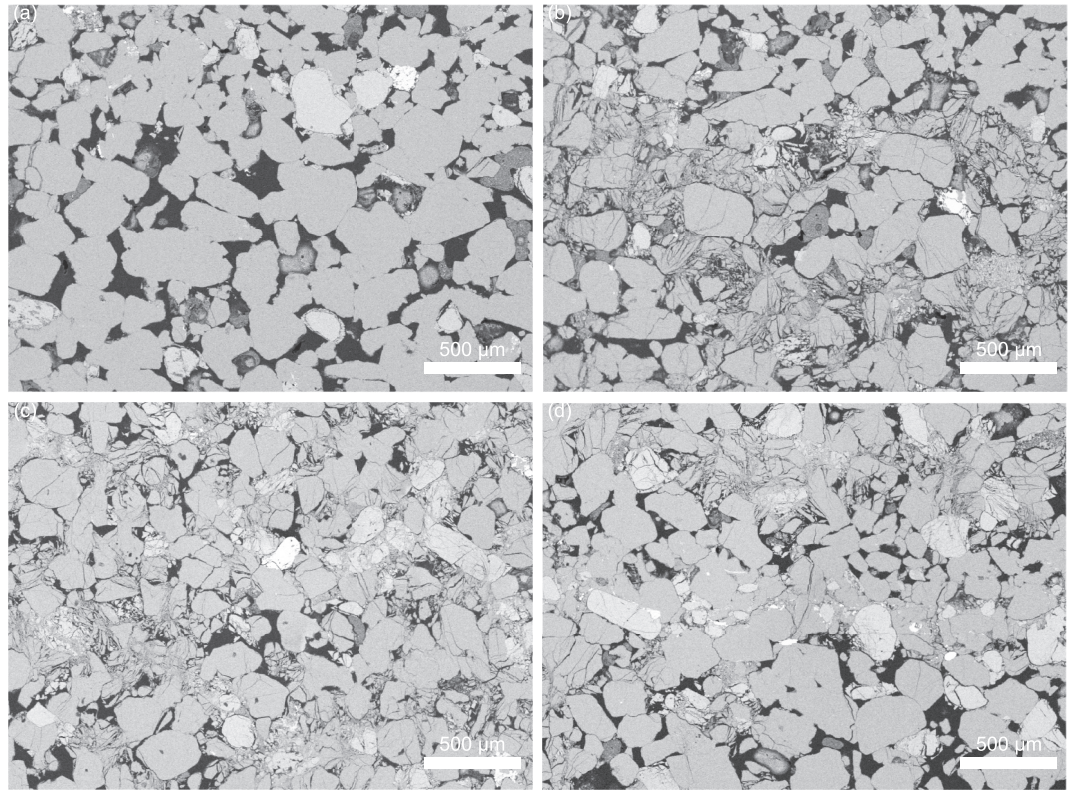

Figure 12. Backscattered electron images of deformed Locharbriggs sandstone. Compression axis is vertical in all images. (a) Relatively intact region in the deformed sample. (b) Isolated compaction band, formed by two connected layers of crushed grains. (c) Compacted region where individual bands cannot be distinguished clearly. (d) Region containing the thin impermeable layer, formed by a locally dense aggregate with interpenetrating grains and fine-grained oxides. Few axial cracks traverse this layer.

The deformed regions in Bleurswiller2 also contain subhorizontal compaction bands, where grains are crushed and pore space is filled with fine-grained particles (Figures 13a and 13b). Individual bands are typically a few mm in length, and form a network running horizontally across the sample. The extent of grain crushing is varied, from just a few axial cracks splitting a grain, up to complete comminution and flow into the pore space. The compaction bands are of few grains in width, that is, from 100 to 400 μm (Figure 13b). Lenses of intact rock, with no visible changes to the pore space, are found between compaction bands. The microstructure of deformed Bleurswiller2 is very similar to that of Bleurswiller1 as documented by Baud et al. (2015).

By contrast with Locharbriggs and Bleurswiller2 sandstones, the deformed Bleurswiller3 sandstone does not display clear discrete compaction bands at the macroscopic scale. At the microscale, the deformed region of the sample (where AEs were located) shows relatively diffuse clusters of crushed grains (Figure 14a), and only a few short (a few mm) isolated subhorizontal bands can be found in the least deformed region (Figure 14b). These observations are in line with our porosity reduction data (Figure 5c) since discrete compaction bands were shown to develop in previous studies with almost 0 radial strain (Baud et al., 2004).

5. Discussion: Spatio-Temporal Relationship Between Compaction and Permeability Change

5.1. Coevolution of Permeability, Wave Speeds, and Acoustic Activity

Our data show that permeability is initially heterogeneous at the cm scale in all the undeformed samples, which is related to the bedding of the sandstones. During deformation, permeability tends to decrease on average, but does so heterogeneously, with some layers experiencing a minimal decrease of the order of a factor 3–5, while other layers see their permeability dropping by a factor 250. The strong heterogeneity in permeability variations is

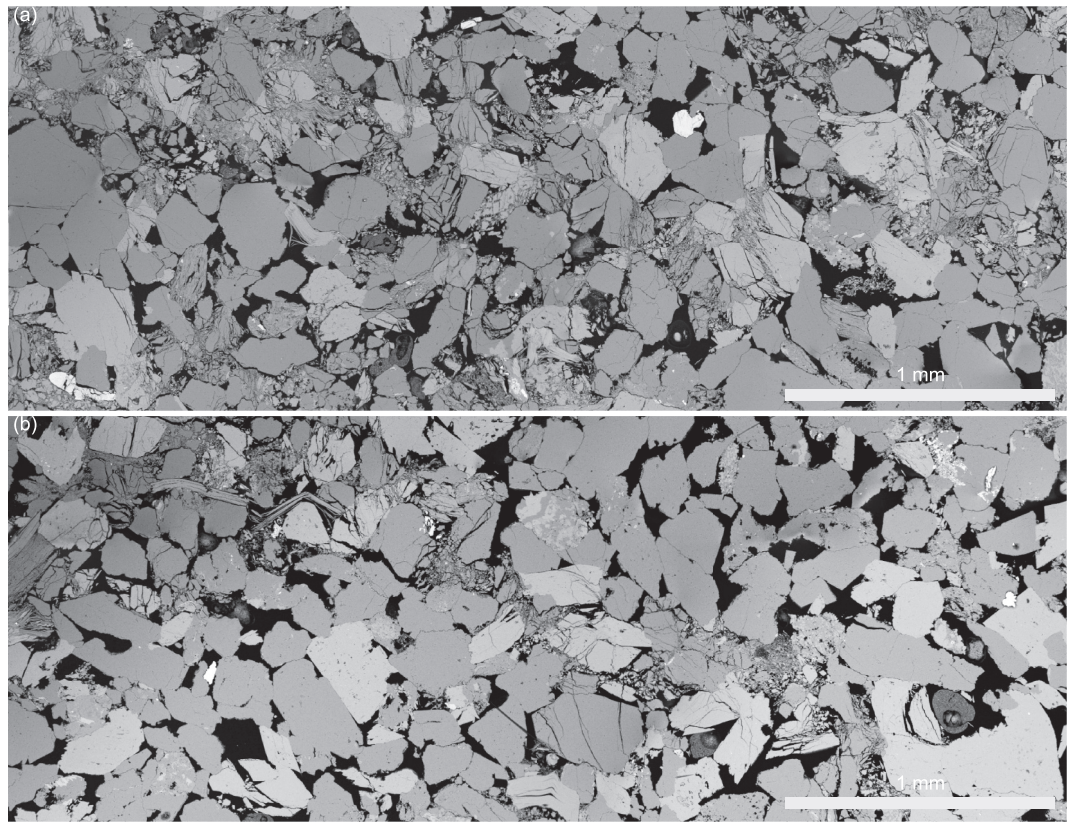

Figure 13. Backscattered electron images of deformed Bleurswiller2 sandstone. Compression axis is vertical. (a) Network of compaction bands in highly deformed region. (b) Isolated compaction band in an otherwise relatively intact matrix.

reflected in both the heterogeneity in (horizontal) wave speed and AE event locations, whereby regions experiencing a strong permeability decrease are also experiencing a strong drop in V_P and a high AE activity. This co-evolution in permeability, wave speed and AE activity is both spatial and temporal. The cumulated AE density in each layer is well correlated with the drop in wave speed, with almost linear trends in all samples (Figure 15). The correlation with permeability change is less systematic: in all tested rocks, there is a clear negative trend, with larger AE densities corresponding to larger permeability decreases, but this trend is not clearly linear or log-linear (Figure 15).

The common mechanism for the observed changes is grain crushing, as seen in the microstructures (Figures 12–14) and in line with all previous observations in porous sandstones (Wong & Baud, 2012, and references therein). Grain crushing is expected to produce acoustic emissions (e.g., Fortin et al., 2006; Olsson & Holcomb, 2000), and reduce effective elastic moduli by replacing equant porosity with denser, but highly fractured aggregates (e.g., Fortin et al., 2007). The resulting decrease in porosity results in a permeability decrease, as previously documented at sample scale (e.g., Baud et al., 2012; Fortin et al., 2005; Zhu & Wong, 1997).

The effect of microcracking on elastic moduli is well described by mean-field approaches, where integrated parameters such as scalar crack density produce smooth variations in elastic properties and thus in wave velocities (e.g., Fortin et al., 2007; Kachanov & Sevostianov, 2012; Sayers & Kachanov, 1995). The "smoothness" of the relationship between crack density parameters and elastic moduli is reflected in the systematic correlation between AE density (as a proxy for crack density) and changes in horizontal V_p (Figure 15).

By contrast, the effect of grain crushing and porosity reduction on permeability is expected to be strongly impacted by the connectivity of the low permeability regions, thus producing threshold effects in the evolution of permeability with increasing deformation. Such effects are observable directly in the spatio-temporal AE distribution during deformation of Locharbriggs and Bleurswiller2 sandstones: it is only when the AE clusters (which correspond to compaction bands) are through-going that a detectable drop in permeability is observed

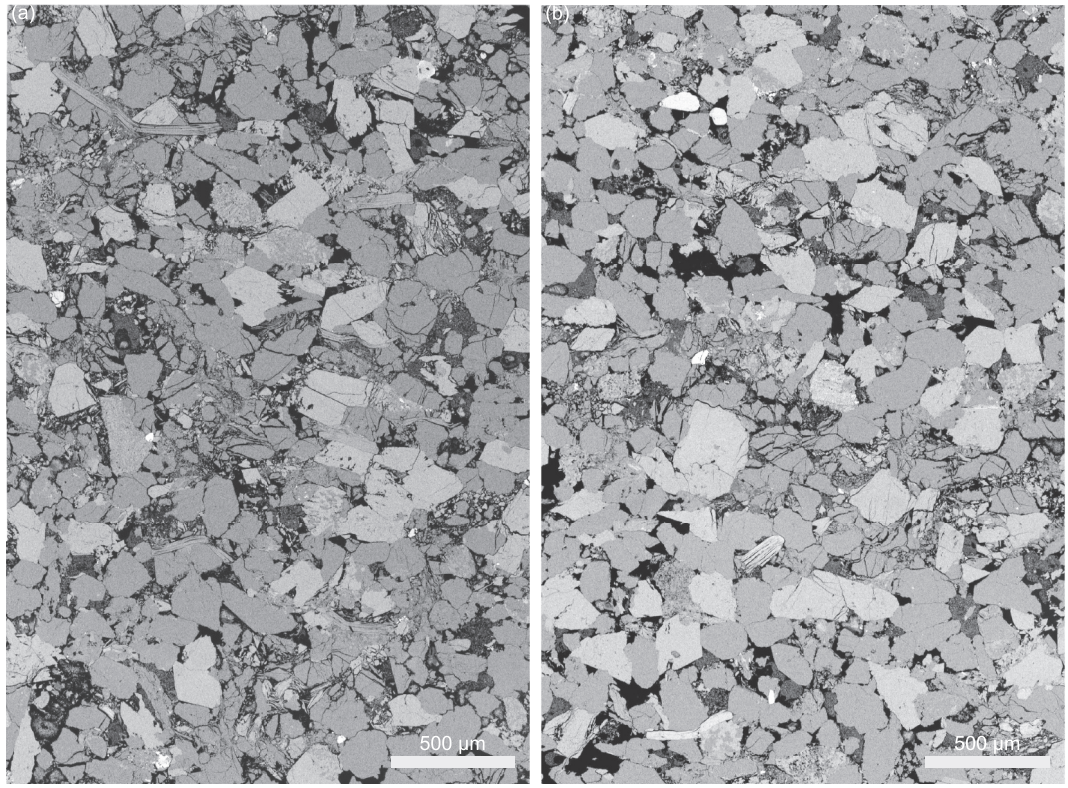

Figure 14. Mosaic of backscattered electron images of deformed Bleurswiller3 sandstone, in two representative regions (a and b). Compression axis is vertical.

across a given layer. This is why AE density is a poor quantitative predictor of the permeability drop, although it is qualitatively following a decreasing trend (Figure 15). An interesting aspect revealed by our data is that permeability seems to decrease more in regions that are initially more permeable than average, so that compaction tends to homogenize or even reverse the permeability structure of the rock. This trend is best observed for the two Bleurswiller sandstones (Figure 16): in both rocks, the initially most permeable layers (2–10 times more than average) experience the strongest decrease in permeability (by factors of 50–250). The trend seems to follow a power law with exponent between −1 and −2. At the scale of our measurements, there is no clear trend in Locharbriggs sandstone. This could be due to the smaller scale bedding heterogeneity of the rock, which leads to thin compaction bands and a lack of representativity of our cm-spaced measurements. For instance, some compaction is clearly identified in the immediate vicinity of the dense, low permeability layer (Figure 12d): this small-scale complexity is not detectable with our measurements.

The stronger permeability decrease in initially higher permeability layers can be explained by the known positive correlation between porosity and permeability (e.g., Mavko et al., 2009, Section 8.4) on one hand, and the negative correlation between porosity and strength (e.g., Wong & Baud, 2012, Section 2) on the other hand. If, due to deposition or diagenetic processes, a given sandstone bed has a higher porosity than its surrounding, it is more prone to yielding and compaction during triaxial deformation. Then, assuming the permeability of compaction bands, once formed, is the same throughout the rock, regardless of the initial state of the material, the potential for permeability decrease is larger in initially more porous (and thus more permeable) layers. Thus, we can arrive at situations where the permeability structure after deformation is reversed compared to the initial state (e.g., Bleurswiller2, Figure 6): the highly permeable layer D compacts first, as evidenced by early AE activity (compared, say, to layer E), and reached a "fully compacted" state with low permeability, controlled by several connected compaction bands, after around 3% strain (similarly to layer B). Meanwhile, layer E remains largely intact, and its permeability is thus larger than that in fully compacted regions.

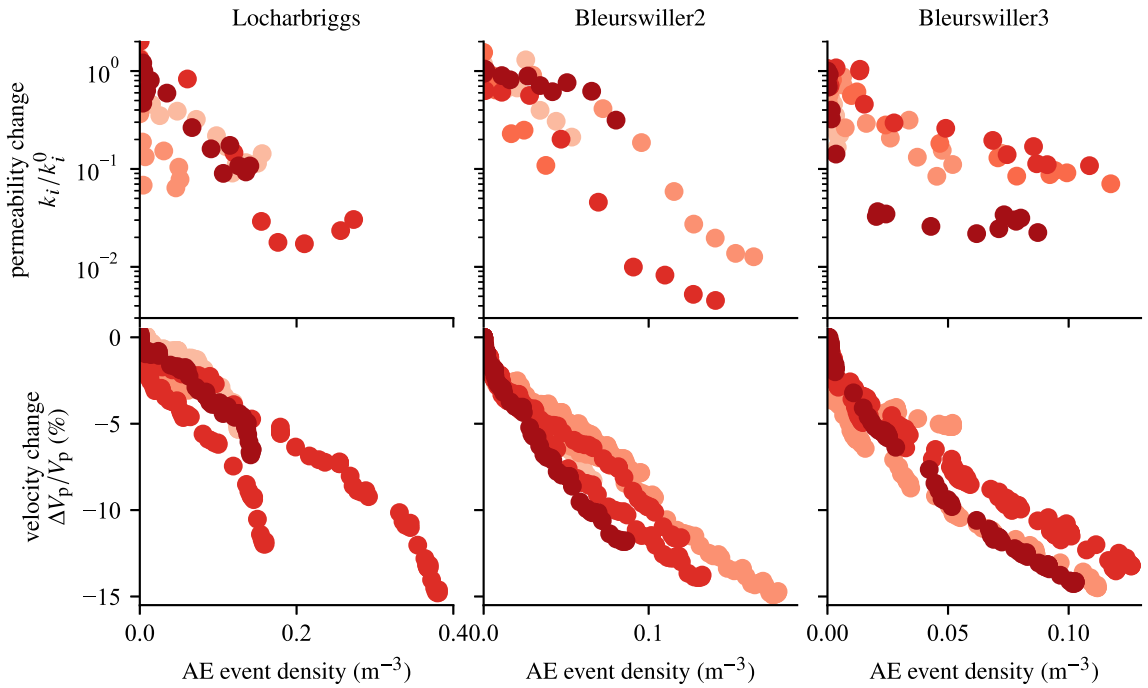

Figure 15. Local permeability and wave velocity variations as functions of AE density in each layer for all tested rocks. The permeability change is reported as the ratio of the current permeability k_i in layer i over the initial permeability k_i^0 in that layer. The wave velocity change is reported at the drop in wave velocity in each layer, normalized by the initial velocity of the layer. Color codes follow those of Figure 6.

5.2. Local Permeability Reduction Due To Local Compaction

Our local measurements allow us to refine previous estimates of the intrinsic permeability k_{cb} of individual compaction bands. In Bentheim sandstone, a 23% porosity, quartz-rich rock, Vajdova et al. (2004) determined k_{cb} ranging from 5×10^{-17} to 2×10^{-16} m^2 (i.e., a reduction by a factor 20–400 compared to the initial matrix permeability), based on an empirical relationship between the measured axial strain, the number of compaction bands, and their sample-scale permeability data. Using a similar method, Baud et al. (2012) determined k_{cb} between 1 and 4×10^{-17} m^2 for compaction bands developing along bedding planes in Diemelstadt sandstone (a 70% quartz, 23% porosity rock).

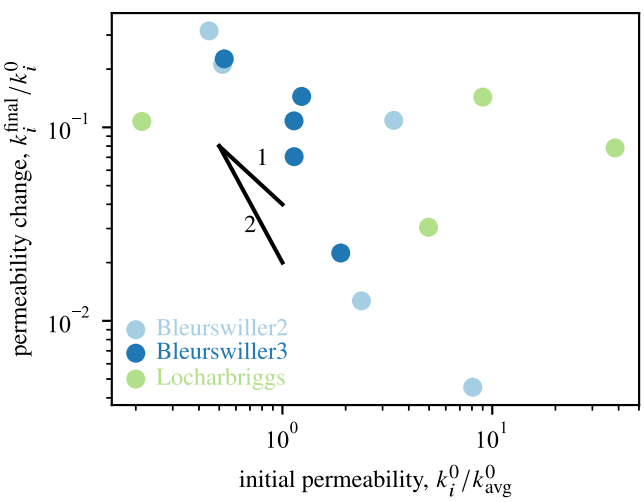

Figure 16. Permeability decrease at the maximum axial strain (3.3%–3.5%) as a function of the initial permeability (normalized by the sample average) for each layer, for the three tested rocks. k_i^0 denotes the initial permeability in layer i, k_{avg}^0 denotes the initial average sample permeability, and k_i^{final} denotes the permeability of layer i at the maximum axial strain for each test. Indicative slopes of 1 and 2 are shown.

For a rock matrix with permeability k_m containing n through-going compaction bands with permeability k_{cb}, the effective permeability perpendicular to the bands is given by

$$k_{eff} = \frac{k_m}{n\ell/L(k_m/k_{cb} - 1) + 1}, \quad (2)$$

where ℓ is the band thickness and L is the total width of the layer containing the bands. The AE distribution and microstructures of our samples indicates that it is difficult, if not impossible, to correctly estimate the exact number of bands at any given stage of deformation; this is in contrast to the aforementioned studies, which used substantially smaller sample sizes and did not have access of in situ monitoring of localized deformation. Thus, we can leave n as unknown and ask ourselves what would be the value of n and k_{cb} required to explain the observed maximum variation in permeability in layers where compaction occurred. We can do this exercise for our three rocks, targeting the layers that experienced the most AE density and permeability drop (Figure 17).

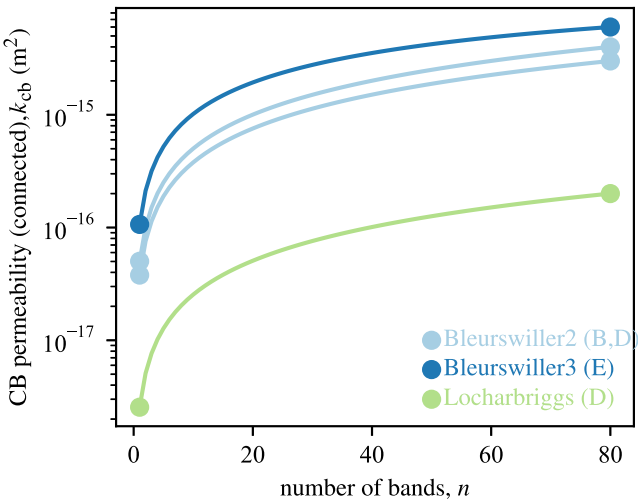

Figure 17. Estimation of the permeability of individual compaction bands, assuming through-going bands, as a function of the possible number of bands in the reported layer (Equation 2). We assumed a band thickness of $\ell = 250\ \mu$m, a layer width of $L = 20$ mm, and the initial matrix permeability k_m is taken as the permeability of the considered layer before deformation.

In Locharbriggs sandstone, where a clear through-going set of bands is observed, we find that the lower bound for k_{cb} is 2.6×10^{-18} m^2, assuming that the entire permeability reduction in layer D is due to a single band. The band permeability k_{cb} becomes 1.0×10^{-17} m^2 and 4.1×10^{-17} m^2 if we consider 4 and 16 bands, respectively. These estimates are in line with those reported in Diemelstadt and Bentheim sandstones.

By contrast, k_{cb} appears to be at least one order magnitude larger in both Bleurswiller2 and Bleurswiller3 sandstones. This is likely not correct, since the microstructure and thickness of the bands in those rocks are very much the same as in Locharbriggs (and in the other sandstones documented in the literature). Rather, what is likely causing this apparent discrepancy is the lack of full connectedness of the compaction bands. Indeed, unlike in Locharbriggs sandstone, there are no clear indications in the AE locations that a single band was completely going through the Bleurswiller2 sample. In Bleurswiller3, AE locations are more distributed and compaction is diffuse at sample scale. In both rocks, microstructures indicate a tortuous network of subhorizontal compaction bands, of a few 100 μm in thickness and a few mm in length. Thus, if we consider compacting rocks as formed by a permeable matrix with a progressively increasing number density of impermeable, elongated, sub-horizontal inclusions (compaction bands), we would expect that the density of inclusions at which a fully connected (percolating) network is formed is actually quite large, typically of the order of 20% (Celzard et al., 1996). In other words, one would need around 20% of rock volume to be occupied by compaction bands for them to form a through-going structure. It is likely that this threshold was not reached in our experiments. In this case, the effective permeability of the compacted rock is expected to decrease less than predicted by Equation 2, due to the existence of a connected network of relatively intact, porous material between the bands.

A complete formulation for the effective permeability of rocks containing disconnected compaction bands remains to be developed.

6. Conclusions

We quantified how porosity and deformation heterogeneities translate into permeability variations at the sub-centimeter scale on three different sandstones. Our results reveal that, depending on the initial microstructure, local variations in permeability (measured in the direction orthogonal to bedding) ranged from a factor of 2 to more than 2 orders of magnitude within the same 10-cm long sample. In particular, significant differences were observed in two samples from the same formation (Bleurswiller sandstone). These variations occur at the sub-centimeter scale and thus are typically not detected in conventional sample-scale permeability measurements. However, they exert a strong control on the mechanical behavior and the deformation-induced evolution of physical properties of these rocks.

Combining acoustic emission, ultrasonic monitoring and local permeability measurements, we showed that compaction localization occurred in the three tested rocks. In Locharbriggs sandstone, we observed the propagation of clear, through-going compaction bands. Upon completion of band propagation across the sample, the average permeability dropped substantially, which is consistent with previous observations by Baud et al. (2012). The permeability drop was the largest (by almost two orders of magnitude) in the region hosting the compaction bands. Such local measurements allowed us to constrain directly the permeability of individual compaction bands, which we find to be of the order of 1 to 4×10^{-17} m^2. In Bleurswiller2 sandstone, we also observed compaction bands associated to local decreases in permeability. However, the bands do not seem to be completely through-going in a connected manner, and the impact on permeability is less than anticipated (by about one order of magnitude; see Figure 17). In Bleurswiller3 sandstone, compaction is observed only in the high porosity part of the sample (spanning approximately 3/4 of the sample length). In that region, compaction is not localized in distinct bands, and permeability decreases progressively with increasing strain.

Despite some clear differences in the deformation localization patterns observed in the three rocks, some common attributes can be outlined. Firstly, our CT and AE data show that inelastic compaction initiated in areas with porosity >20% and with permeability between 10^{-14} and 10^{-12} m^2. By contrast, minimal AE activity and permeability variations occurred in areas with initial porosity <20%. Secondly, our microstructural observations revealed that grain crushing in clusters of different shapes and sizes developed in all samples. In Locharbriggs and Bleurswiller2 sandstones, these clusters form subhorizontal compaction bands similar to those reported by Baud et al. (e.g., 2004); Fortin et al. (e.g., 2006): within a width of the order of 0.5 mm (2 and 3 grains), all grains are strongly comminuted, and porosity is filled with the crushed material. In Bleurswiller3 sandstone, grain crushing appears more distributed, at least in the regions that experienced large axial deformation, but the grain-scale microstructure appears similar to that of compaction bands in the other tested rocks.

For all samples, in the zones where maximum compaction was observed, a reduction of permeability by a factor of around 100 was associated to a reduction in P wave velocity by around 10%–15%, which is consistent with the role of microcracking in the compaction process.

Taken together, our results show that the impact of compactant deformation on permeability in sandstone is controlled by (a) the microscale characteristics of the crushed regions (infilling of pore space by crushed materials), and (b) the connectivity of these crushed regions across the flow direction.

Data Availability Statement

The raw and processed data can be obtained from Zenodo Brantut and Baud (2024).

Acknowledgments

Neil Hughes provided technical support on the triaxial apparatus. Ian Wood conducted the x-ray diffraction analysis of the starting material. Jim Davy supported us with the operation of the Scanning Electron Microscope at UCL. We also thank Phil Meredith and Teng-Fong Wong for useful discussions in the course of this work. NB gratefully acknowledges financial support from the UK Natural Research Council (Grant NE/S000852/1) and the European Research Council under the European Union's Horizon 2020 research and innovation programme (project RockDEaF, grant agreement 804685). This work of the Interdisciplinary Thematic Institute Geosciences for the energy system transition, as part of the ITI 2021–2028 program of the University of Strasbourg, CNRS and Inserm, was supported by IdEx Unistra (ANR-10-IDEX-0002), and by SFRI-STRAT'US project (ANR-20-SFRI-0012) under the framework of the French Investments for the Future Program.

References

Abdallah, Y., Sulem, J., Bornert, M., Ghabezloo, S., & Stefanou, I. (2020). Compaction banding in high porosity carbonate rocks: 1. Experimental observations. *Journal of Geophysical Research: Solid Earth*, *126*, e2020JB020538. https://doi.org/10.1029/2020JB020538

Aydin, A., & Ahmadov, R. (2009). Bed-parallel compaction bands in aeolian sandstone: Their identification, characterization and implications. *Tectonophysics*, *479*(3–4), 277–284. https://doi.org/10.1016/j.tecto.2009.08.033

Barraclough, T. W., Blackford, R., Liebenstein, S., Sandfled, S., Stratford, T. J., Weinländer, G., & Zaiser, M. (2017). Propagating compaction bands in confined compression of snow. *Nature Physics*, *13*(3), 272–275. https://doi.org/10.1038/nphys3966

Bastawros, A., Bart-Smith, B., & Evans, A. G. (2000). Experimental analysis of deformation mechanisms in a closed-cell alumninum alloy foam. *Journal of the Mechanics and Physics of Solids*, *48*(2), 301–322.

Baud, P., Klein, E., & Wong, T.-F. (2004). Compaction localization in porous sandstones: Spatial evolution of damage and acoustic emission activity. *Journal of Structural Geology*, *26*(4), 603–624. https://doi.org/10.1016/j.jsg.2003.09.002

Baud, P., Meredith, P. G., & Townend, E. (2012). Permeability evolution during triaxial compaction of an anisotropic porous sandstone. *Journal of Geophysical Research*, *117*(B5), B05203. https://doi.org/10.1029/2012JB009176

Baud, P., Reuschlé, T., Ji, Y., Cheung, C. S., & Wong, T.-F. (2015). Mechanical compaction and strain localization in Bleurswiller sandstone. *Journal of Geophysical Research: Solid Earth*, *120*(9), 6501–6522. https://doi.org/10.1002/2015jb012192

Baud, P., Schubnel, A., Heap, M. J., & Rolland, A. (2017). Inelastic compaction in high porosity limestone monitored using acoustic emissions. *Journal of Geophysical Research: Solid Earth*, *122*(12), 9989–10009. https://doi.org/10.1002/2017jb014627

Brantut, N. (2018). Time-resolved tomography using acoustic emissions in the laboratory, and application to sandstone compaction. *Geophysical Journal International*, *213*(3), 2177–2192. https://doi.org/10.1093/gji/ggy068

Brantut, N. (2020). Dilatancy-induced fluid pressure drop during dynamic rupture: Direct experimental evidence and consequences for earthquake dynamics. *Earth and Planetary Science Letters*, *538*, 116179. https://doi.org/10.1016/j.epsl.2020.116179

Brantut, N., & Aben, F. M. (2021). Fluid pressure heterogeneity during fluid flow in rocks: New laboratory measurement device and method. *Geophysical Journal International*, *225*(2), 968–983. https://doi.org/10.1093/gji/ggab019

Brantut, N., & Baud, P. (2024). Permeability, acoustic emission and velocities during compaction of porous sandstone [Dataset]. *Zenodo*. https://doi.org/10.5281/zenodo.12793855

Carbillet, L., Heap, M. J., Baud, P., Wadsworth, F. B., & Reuschlé, T. (2021). Mechanical compaction of crustal analogs made of sintered glass beads: The influence of porosity and grain size. *Journal of Geophysical Research: Solid Earth*, *126*(4), e2020JB021321. https://doi.org/10.1029/2020JB021321

Carbillet, L., Heap, M. J., Baud, P., Wadsworth, F. B., & Reuschlé, T. (2022). The influence of grain size distribution on mechanical compaction and compaction localization in porous rocks. *Journal of Geophysical Research: Solid Earth*, *127*(11), e2022JB025216. https://doi.org/10.1029/2022JB025216

Celzard, A., McRae, E., Deleuze, C., Dufort, M., Furdin, G., & Marêché, J.-M. (1996). Critical concentration in percolating systems containing a high-aspect-ratio filler. *Physical Review B: Condensed Matter*, *53*(10), 6209–6214. https://doi.org/10.1103/physrevb.53.6209

Charalampidou, E., Hall, S. A., Stanchits, S., Lewis, H., & Viggiani, G. (2011). Characterization of shear and compaction bands in a porous sandstone deformed under triaxial compression. *Tectonophyiscs*, *503*(1–2), 8–17. https://doi.org/10.1016/j.tecto.2010.09.032

Chen, X., Regenauer-Lieb, K., Lv, A., Hu, M., & Roshan, H. (2020). The dynamic evolution of permeability in compacting carbonates: Phase transition and critical points. *Transport in Porous Media*, *135*(3), 687–711. https://doi.org/10.1007/s11242-020-01493-y

Chen, X., Roshan, H., Lv, A., Hu, M., & Regenauer-Lieb, K. (2020). The dynamic evolution of compaction bands in highly porous carbonates: The role of local heterogeneity for nucleation and propagation. *Progress in Earth and Planetary Science*, *7*(1), 28. https://doi.org/10.1186/s40645-020-00344-0

Cheung, C., Baud, P., & Wong, T. (2012). Effect of grain size distribution on the development of compaction localization in porous sandstone. *Geophysical Research Letters*, *39*(21), L21302. https://doi.org/10.1029/2012GL053739

Deng, S., Zuo, L., Aydin, A., Dvorkin, J., & Mukerji, T. (2015). Permeability characterization of natural compaction bands using core flooding experiments and three-dimensional image-based analysis: Comparing and contrasting the results from two different methods. *AAPG Bulletin*, *99*(1), 27–49. https://doi.org/10.1306/07071413211

Eccles, D., Sammonds, P. R., & Clint, O. C. (2005). Laboratory studies of electrical potential during rock fracture. *International Journal of Rock Mechanics and Mining Sciences*, *42*(7–8), 933–949. https://doi.org/10.1016/j.ijrmms.2005.05.018

Fortin, J., Guéguen, Y., & Schubnel, A. (2007). Effects of pore collapse and grain crushing on ultrasonic velocities and Vp/Vs. *Journal of Geophysical Research*, *112*(B8), B08207. https://doi.org/10.1029/2005JB004005

Fortin, J., Schubnel, A., & Guéguen, Y. (2005). Elastic wave velocities and permeability evolution during compaction of bleurswiller sandstone. *International Journal of Rock Mechanics and Mining Sciences*, *42*(7–8), 873–889. https://doi.org/10.1016/j.ijrmms.2005.05.002

Fortin, J., Stanchits, S., Dresen, G., & Guéguen, Y. (2006). Acoustic emission and velocities associated with the formation of compaction bands in sandstone. *Journal of Geophysical Research*, *111*(B10), B10203. https://doi.org/10.1029/2005JB003854

Fossen, H., Schultz, R. A., & Torabi, A. (2011). Conditions and implications for compaction band formation in the Navajo sandstone, Utah. *Journal of Structural Geology*, *33*(10), 1477–1490. https://doi.org/10.1016/j.jsg.2011.08.001

Heap, M. J., Brantut, N., Baud, P., & Meredith, P. G. (2015). Time-dependent compaction band formation in sandstone. *Journal of Geophysical Research: Solid Earth*, *120*(7), 4808–4830. https://doi.org/10.1002/2015JB012022

Hill, R. E. (1989). *Analysis of deformation bands in the Valley of Fire State Park, Nevada* (MS Thesis). University of Nevada, 68 p.

Holcomb, D. J., & Olsson, W. A. (2003). Compaction localization and fluid flow. *Journal of Geophysical Research*, *108*(B6), 2290. https://doi.org/10.1029/2001JB000813

Jefferd, M., Brantut, N., Meredith, P. G., Mitchell, T. M., & Plümper, O. (2021). Compactive deformation of sandstone under crustal pressure and temperature conditions. *Journal of Geophysical Research: Solid Earth*, *126*(4), e2020JB020202. https://doi.org/10.1029/2020JB020202

Kachanov, M., & Sevostianov, I. (2012). Rice's internal variables formalism and its implications for the elastic and conductive properties of cracked materials, and for the attempts to relate strength to stiffness. *Journal of Applied Mechanics*, *79*(3), 031002. https://doi.org/10.1115/1.4005957

Liu, C., Pollard, D. D., Gu, K., & Shi, B. (2015). Mechanism of formation of wiggly compaction bands in porous sandstone: 2. Numerical simulation using discrete element method. *Journal of Geophysical Research: Solid Earth*, *120*(12), 8153–8168. https://doi.org/10.1002/2015JB012374

Loaiza, S., Fortin, J., Schubnel, A., Guéguen, Y., Vinciguerra, S., & Moreira, M. (2012). Mechanical behaviour and localized failure modes in a porous basalt from the Azores. *Geophysical Research Letters*, *39*(19), L19304. https://doi.org/10.1029/2012GL053218

Louis, L., Baud, P., & Wong, T.-F. (2009). Microstructural inhomogeneity and mechanical anisotropy associated with bedding in Rothbach sandstone. *Pure and Applied Geophysics*, *166*, 1063–1087. https://doi.org/10.1007/978-3-0346-0122-1_15

Mavko, G., Mukerji, T., & Dvorkin, J. (2009). *The rock physics handbook* (2nd ed.). Cambridge University Press.

Menéndez, B., Zhu, W., & Wong, T.-F. (1996). Micromechanics of brittle faulting and cataclastic flow in Brea sandstone. *Journal of Structural Geology*, *18*(1), 1–16. https://doi.org/10.1016/0191-8141(95)00076-p

Meng, F., Huang, L., Baud, P., & Wong, T. (2023). Strain localization in 4D imaged by X-ray computed tomography and digital volume correlation: Discrete compaction bands in Leitha limestone. *Journal of the Mechanics and Physics of Solids*, *171*, 105–160. https://doi.org/10.1016/j.jmps.2022.105160

Mollema, P. N., & Antonellini, M. A. (1996). Compaction bands: A structural analog for anti-mode I cracks in aeolian sandstone. *Tectonophysics*, *267*(1–4), 209–228. https://doi.org/10.1016/s0040-1951(96)00098-4

Olsson, W. A., & Holcomb, D. J. (2000). Compaction localization in porous rock. *Geophysical Research Letters*, *27*(21), 3537–3540. https://doi.org/10.1029/2000gl011723

Papka, S. D., & Kyriakides, S. (1999). Biaxial crushing of honeycombs: –Part 1: Experiments. *International Journal of Solids and Structures*, *36*(29), 4367–4396. https://doi.org/10.1016/s0020-7683(98)00224-8

Rice-Birchall, E., Faulkner, D. R., & Bedford, J. D. (2022). The effect of grain size and porosity on the nature of compaction localisation in high-porosity sandstone. *Journal of Structural Geology*, *164*, 104–740. https://doi.org/10.1016/j.jsg.2022.104740

Rotevatn, A., Thorsheim, E., Bastesen, E., Fossmark, H. S. S., Torabi, A., & len, G. S. (2016). Sequential growth of deformation bands in carbonate grainstones in the hangingwall of an active growth fault: Implications for deformation mechanisms in different tectonic regimes. *Journal of Structural Geology*, *90*, 27–47. https://doi.org/10.1016/j.jsg.2016.07.003

Sammis, C. G., King, G., & Biegel, R. (1987). The kinematics of gouge deformation. *Pure and Applied Geophysics*, *125*(5), 777–812. https://doi.org/10.1007/bf00878033

Sayers, C., & Kachanov, M. (1995). Microcrack-induced elastic wave anisotropy of brittle rocks. *Journal of Geophysical Research*, *100*(B3), 4149–4156. https://doi.org/10.1029/94jb03134

Schultz, R. A., Okubo, C. H., & Fossen, H. (2010). Porosity and grain size controls on compaction band formation in Jurassic Navajo Sandstone. *Geophysical Research Letters*, *37*(22), L22306. https://doi.org/10.1029/2010GL044909

Sleeman, R., & van Eck, T. (1999). Robust automatic P-phase picking: An on-line implementation in the analysis of broadband seismogram recordings. *Physics of the Earth and Planetary Interiors*, *113*(1–4), 265–275. https://doi.org/10.1016/s0031-9201(99)00007-2

Sternlof, K. R. (2005). *Structural geology, propagation mechanics and hydraulic effects of compaction bands in sandstone* (Ph.D. Thesis). Stanford University.

Sun, W., Andrade, J. E., Rudnicki, J. W., & Eichhubl, P. (2011). Connecting microstructural attributes and permeability from 3D tomographic images of in situ shear-enhanced compaction bands using multiscale computations. *Geophysical Research Letters*, *38*(10), L10302. https://doi.org/10.1029/2011GL047683

Tembe, S., Baud, P., & Wong, T. (2008). Stress conditions for the propagation of discrete compaction bands in porous sandstone. *Journal of Geophysical Research*, *113*(B9), B09409. https://doi.org/10.1029/2007JB005439

Tondi, E., Cilona, A., Agosta, F., Aydin, A., Rustichelli, A., Renda, P., & Giunta, G. (2012). Growth processes, dimensional parameters and scaling relationships of two conjugate sets of compactive shear bands in porous carbonate grainstones, Favignana Island, Italy. *Journal of Structural Geology*, *37*, 53–64. https://doi.org/10.1016/j.jsg.2012.02.003

Townend, E., Thompson, B. D., Benson, P. M., Meredith, P. G., Baud, P., & Young, R. P. (2008). Imaging compaction band propagation in Diemelstadt sandstone using acoustic emission locations. *Geophysical Research Letters*, *35*(15), L15301. https://doi.org/10.1029/2008GL034723

Vajdova, V., Baud, P., & Wong, T.-F. (2004). Permeability evolution during localized deformation in Bentheim sandstone. *Journal of Geophysical Research*, *109*(B10406). https://doi.org/10.1029/2003JB002942

Wang, B., Chen, Y., & Wong, T. (2008). A discrete element model for the development of compaction localization in granular rock. *Journal of Geophysical Research*, *113*(B3), B03202. https://doi.org/10.1029/2006JB004501

Wong, T.-F., & Baud, P. (2012). The brittle-ductile transition in porous rock: A review. *Journal of Structural Geology*, *44*, 25–53. https://doi.org/10.1016/j.jsg.2012.07.010

Wong, T. F., David, C., & Zhu, W. (1997). The transition from brittle faulting to cataclastic flow in porous sandstones: Mechanical deformation. *Journal of Geophysical Research*, *102*(B2), 3009–3025. https://doi.org/10.1029/96jb03281

Wu, X. Y., Baud, P., & Wong, T.-F. (2000). Micromechanics of compressive failure and spatial evolution of anisotropic damage in Darley Dale sandstone. *International Journal of Rock Mechanics and Mining Sciences*, *37*(1–2), 143–160. https://doi.org/10.1016/s1365-1609(99)00093-3

Zhu, W., Montesi, L., & Wong, T.-F. (1997). Shear-enhanced compaction and permeability reduction: Triaxial extension tests on porous sandstone. *Mechanics of Materials*, *25*(3), 197–225. https://doi.org/10.1016/s0167-6636(97)00011-2

Zhu, W., & Wong, T.-F. (1997). The transition from brittle faulting to cataclastic flow: Permeability evolution. *Journal of Geophysical Research*, *102*(B2), 3027–3041. https://doi.org/10.1029/96jb03282